AFRL-RQ-WP-TR-2012-0247

SUPERSONIC COMBUSTION RAMJET RESEARCH

Campbell D. Carter

Propulsion Sciences Branch
Aerospace Propulsion Division

AUGUST 2012
Final Report

AIR FORCE RESEARCH LABORATORY
AEROSPACE SYSTEMS DIRECTORATE
WRIGHT-PATTERSON AIR FORCE BASE, OH 45433-7542
AIR FORCE MATERIEL COMMAND
UNITED STATES AIR FORCE

NOTICE AND SIGNATURE PAGE

AFRL-RQ-WP-TR-2012-0247 HAS BEEN REVIEWED AND IS APPROVED FOR PUBLICATION IN ACCORDANCE WITH ASSIGNED DISTRIBUTION STATEMENT.

*//Signature//

CAMPBELL D. CARTER
Program Manager
Propulsion Sciences Branch

//Signature//

MARK A. AMENDT, Chief
Propulsion Sciences Branch
Aerospace Propulsion Division

//Signature//

THOMAS A. JACKSON, Chief
Aerospace Propulsion Division
Aerospace Systems Directorate

*Disseminated copies will show “//Signature//” stamped or typed above the signature blocks.

REPORT DOCUMENTATION PAGE

Form Approved
OMB No. 0704-0188

1. REPORT DATE *(DD-MM-YY)*
August 2012

2. REPORT TYPE
Final

3. DATES COVERED *(From - To)*
01 May 2004 – 30 April 2012

4. TITLE AND SUBTITLE
SUPERSONIC COMBUSTION RAMJET RESEARCH

5a. CONTRACT NUMBER
In-house

5b. GRANT NUMBER

5c. PROGRAM ELEMENT NUMBER
61102F

6. AUTHOR(S)
Campbell D. Carter

5d. PROJECT NUMBER
2308

5e. TASK NUMBER

5f. WORK UNIT NUMBER
Q0EF

7. PERFORMING ORGANIZATION NAME(S) AND ADDRESS(ES)
Propulsion Sciences Branch (AFRL/RQHS)
Aerospace Propulsion Division
Air Force Research Laboratory, Aerospace Systems Directorate
Wright-Patterson Air Force Base, OH 45433-7542
Air Force Materiel Command, United States Air Force

8. PERFORMING ORGANIZATION REPORT NUMBER
AFRL-RQ-WP-TR-2012-0247

9. SPONSORING/MONITORING AGENCY NAME(S) AND ADDRESS(ES)
Air Force Research Laboratory
Aerospace Systems Directorate
Wright-Patterson Air Force Base, OH 45433-7542
Air Force Materiel Command
United States Air Force

10. SPONSORING/MONITORING AGENCY ACRONYM(S)
AFRL/RQHS

11. SPONSORING/MONITORING AGENCY REPORT NUMBER(S)
AFRL-RQ-WP-TR-2012-0247

12. DISTRIBUTION/AVAILABILITY STATEMENT
Approved for public release; distribution unlimited.

13. SUPPLEMENTARY NOTES
PA Case Number: 88ABW-2012-4228; Clearance Date: 03 Aug 2012. This report contains color.

14. ABSTRACT

This basic research task on supersonic combustion ramjets includes work in three primary focus areas: 1) fuel control and fuel injection, wherein fundamental aspects are studied for gaseous, supercritical, and multiphase fuels; 2) ignition, flameholding, and flame propagation in supersonic flows, wherein fundamental aspects are studied with a view toward improving performance in a high-speed combustor; and 3) multidisciplinary laser measurements for benchmarking modeling and simulation and for elucidating the physics of high-speed flows. The motivation for this program is the need to develop the science basis to enable the design of high-speed, air-breathing propulsion systems.

15. SUBJECT TERMS
high-speed propulsion scramjet propulsion; fuel injection and mixing; scramjet flameholding; laser diagnostics

16. SECURITY CLASSIFICATION OF:

a. REPORT	**b. ABSTRACT**	**c. THIS PAGE**	**17. LIMITATION OF ABSTRACT:**	**18. NUMBER OF PAGES**
Unclassified	Unclassified	Unclassified	SAR	58

19a. NAME OF RESPONSIBLE PERSON (Monitor)
Campbell D. Carter

19b. TELEPHONE NUMBER *(Include Area Code)*
N/A

TABLE OF CONTENTS

Section Page

LIST OF FIGURES

1 SUMMARY

This basic research task on supersonic combustion ramjets includes work in three primary focus areas:

1. ***Fuel Control and Fuel Injection***, wherein fundamental aspects are studied for gaseous, supercritical, and multiphase fuels;
2. ***Ignition, Flameholding, and Flame Propagation in Supersonic Flows***, wherein fundamental aspects are studied with a view towards improving performance in a high-speed combustor; and
3. ***Multidisciplinary Laser Measurements*** for benchmarking modeling and simulation and for elucidating the physics of high-speed flows.

Within each of these areas, there is a strong relevance to the scramjet propulsion system, and that relationship helps frame the context of our research. The motivation for this program is the need to develop the science basis to enable the design of high-speed, air-breathing propulsion systems. Lack of a science basis (and, in general, technology basis) is a limiting factor in design of scramjet vehicles. This final report is organized along the lines of the primary focus areas, but it should be noted that the report as follows is only a summary of a large body of research. The primary product of this effort is the knowledge base contained with the research papers, which are listed in the References Section. The reader is encouraged to look at these documents for an in-depth description of the work from this program.

2 INTRODUCTION

2.1 Background

The motivation for this program is the need for a strong science basis to enable the understanding and design of high-speed, air-breathing propulsion systems. The goals of this research have been to investigate critical aspects of the supersonic combustion ramjet (scramjet) engine and to build a science basis for scaling up engines flowpaths from their current 1-X scales (defined here as 5 kg/s of air flow) to 10-X scales. There are three primary focus areas within the Supersonic Combustion Ramjet Basic Research task that intended to provide a strong science basis for high-speed propulsion.

1. *Fuel Control and Fuel Injection:* fundamental aspects of fuel control and injection are studied for gaseous, supercritical, and multiphase fuels.
2. *Ignition, Flameholding, and Flame Propagation in Supersonic Flows*: fundamental aspects of ignition, flameholding, and flamespreading are studied. This portion of the program includes both simplified laboratory studies and more complex studies in high-speed ducts.
3. *Multidisciplinary Laser Measurements*: advanced diagnostics methods are developed and employed to further our understanding of issues relevant to high-speed flight and to provide benchmark data for the improvement of numerical tools.

This *Scramjet Research* effort leverages diagnostic, computational, and experimental assets within AFRL/RQH (and elsewhere)—that together form a unique fundamental research environment—to examine a phenomenon in its full complexity, after it has been distilled into its more basic pieces.

2.2 Approach

The focus for this work has been on experimentation to elucidate the physics of phenomena relevant to high-speed flows for a supersonic combustion ramjet engine. Not every piece of work described within this report has direct relevance to high-speed propulsion (e.g., measurements in a subsonic, co-axial jet to better understand mixing), but all the work has relevance to some aspect of mixing, combustion, or propulsion that in turn has relevance to high-speed propulsion. Within this work there has been a heavy emphasis on the development and application of advanced laser diagnostics. This has been one of our primary objectives: to better understand the physics of flows using nonintrusive measurements.

2.3 Scope

The scope for this program has been broad. While the explicit focus has been on advancement of our knowledge base, to enable scramjet engine design, a broad range of experiments (primarily) and computations have been conducted on fuel-air mixing, fuel injection (particularly for high-speed flows), plasma-assisted combustion, flameholding (particularly in a high-speed flow), and development and application of diagnostic methods. The experiments have been designed both to advance our understanding of specific phenomena, such as flameholding in a scramjet flowpath, and to provide experimental data for advancement of computational fluid dynamic (CFD) simulation capability. It should be noted that in executing this eight-year program, we have actively interacted with the university research community. Indeed, many of the research efforts have involved students working on graduate degrees, and there has been a concerted effort to reach out to the community performing relevant, related research.

3 METHODS, ASSUMPTIONS, AND PROCEDURES

As noted, this report is primarily a description of experimental research results. We have used facilities available to AFRL/RQHS that include supersonic windtunnels (in Research Cells 18, 19, and 22) and optics laboratories. Furthermore, we have explored the use of innovative optical diagnostic methods to better understand the physics of flows relevant to high-speed propulsion. These optical techniques include, but are not limited to, laser-induced fluorescence (LIF and the related technique planar LIF, also known as PLIF), Rayleigh scattering, spontaneous Raman scattering, particle image velocimetry (PIV), hydroxyl tagging velocimetry (HTV), and pressure sensitive paint (PSP). We have also explored X-ray techniques to probe optically dense sprays (relevant to fuel sprays); this work has been done at the Advanced Photon Source (APS), Argonne National Laboratory (ANL). Finally, we have explored high-frequency diagnostics, including kHz-rate PIV and PLIF. This work has been done in conjunction with the German Aerospace Center (DLR), in Stuttgart, primarily, but more recently these same techniques have implemented at AFRL. Indeed, we have now applied kHz-rate PLIF of hydroxyl (OH) and nitric oxide (NO) at AFRL facilities (including the Research Cell 19 windtunnel).

4 RESULTS AND DISCUSSION

This section discusses results from this eight-year program. It is organized along the focus areas:

1. Fuel Control and Fuel Injection;
2. Ignition, Flameholding, and Flame Propagation in Supersonic Flows; and
3. Multidisciplinary Laser Measurements.

As noted above the conference papers (and posters) and journal papers listed in the reference section represent to complete history and accomplishments of this program. Here, references are listed chronologically, rather than by focus area.

4.1 Fuel Control and Fuel Injection

Fuel injection into a supersonic crossflow is a critical aspect of a successful scramjet propulsion system. As such, fundamental studies of fuel injection have been a significant part of this and other AFOSR-funded research, and substantial insight into the process has yielded successful scramjet injector designs, as well as fundamental data on injection into a supersonic crossflow. A sample set of images describing a study of a diamond-shaped injector is shown in Figure 1 (see Refs. 32, 33, 52); this work was conducted in our 130 × 152 mm^2 windtunnel (Research Cell 19). Here, planar laser-induced fluorescence (PLIF) of the nitric oxide (NO)

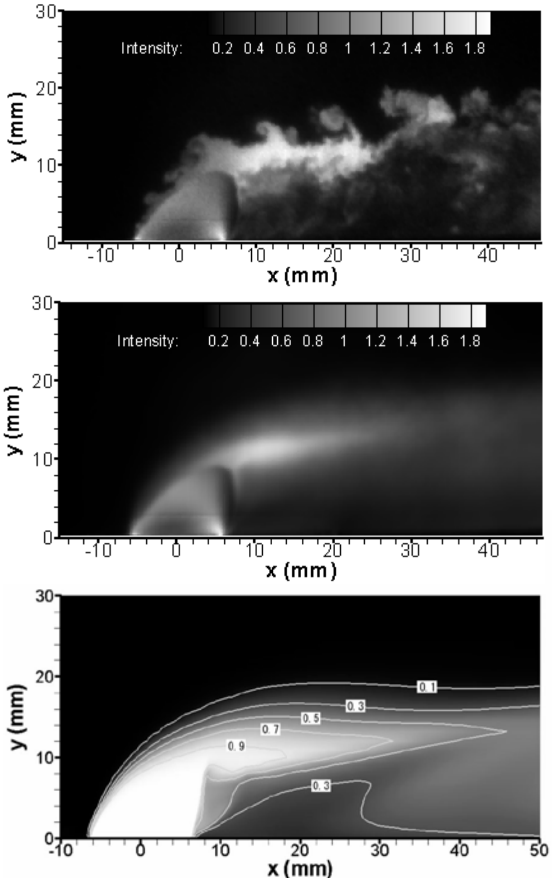

Figure 1: Instantaneous (TOP) and Frame-Averaged NO PLIF (Middle) and Computations of Jet Mole Fraction from Diamond-Shaped Injector (Bottom) [33].

molecule, which is added to air in trace concentration, was used to mark an injectant that issues into a Mach-2 crossflow (an approach that is discussed in more detail below); both instantaneous and frame-averaged images are shown along with a computation of injectant mole fraction from a Reynolds-averaged Navier-Stokes (RANS) computational fluid dynamics (CFD) model.

4.1.1 Supercritical Fuel Injection

Injection of a supercritical fluid into a superheated, low-pressure, high-speed crossflow—a problem relevant to much of the scramjet flight envelope—is vital to the scramjet, yet poorly understood. Extensive studies conducted in this laboratory have shown that the plume structure of supercritical fuel jets can be dramatically different from those of liquid or gaseous jets, due to the unique thermodynamic properties of the supercritical fluid and the occurrence of condensation. Typically, supercritical jets behave like ideal-gas jets when the injection temperatures are not too close to the critical temperature. A two-phase jet with a large quantity of nucleated droplets, however, can be generated, presumably through the homogeneous nucleation process, if the injection temperature is close to the critical temperature, as demonstrated in Figure 2. Clearly, the liquid content within the jet indicates that a relatively long length/time will be needed for the injectant to reach the desired fuel/air mixing, and the issue of relevance to the scramjet designer is what methodologies/techniques will be needed to efficiently and smoothly handle the continuously changing fuel state.

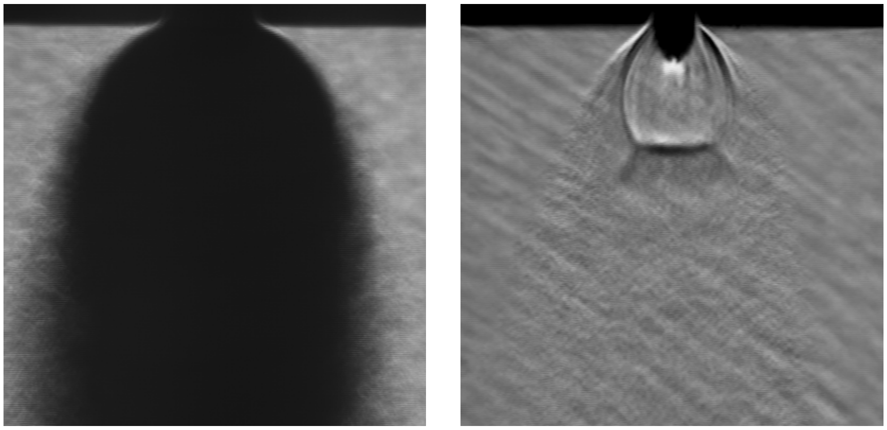

P_{inj}/P_c =	1.16	1.15
T_{inj}/T_c =	1.03	1.23

Figure 2: Shadowgraph for CH_4/C_2H_6 Jets at Two Injection Temperatures.

X_{CH4}=0.1 and d=1.0 mm.

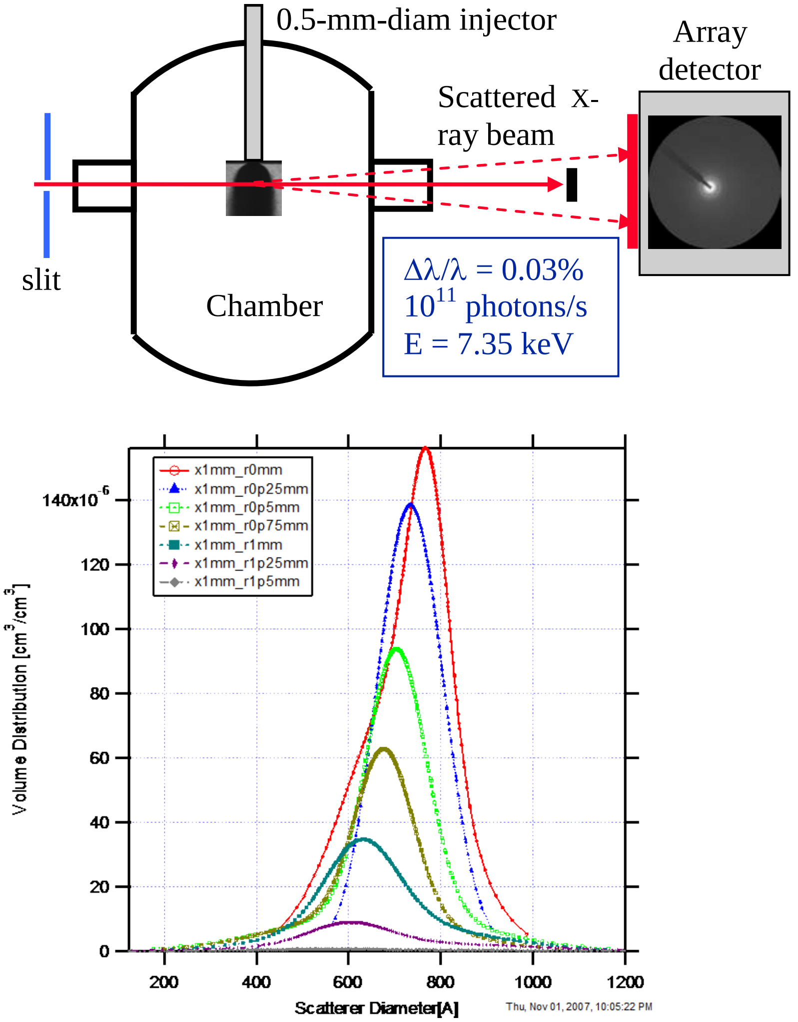

Figure 3: Setup for Small-Angle X-Ray Scattering (Top) and Sample Droplet Volume Distributions Versus Jet Radius (Bottom).

Conditions for volume distribution are T_{inj} = 285 K and P_{inj} = 5.15 MPa; x=1.0 mm.

While much early work had been done to understand injection of a supercritical fuel (and the condensation process), early in 2007 an effort was begun to probe condensing, supercritical ethylene (C_2H_4) jets using X-rays, teaming with personnel at the Advanced Photon Source (APS), Argonne National Laboratory. The technique chosen was small-angle X-ray scattering, SAXS, which is shown schematically in Figure 3; the work was conducted in the 8-ID beamline. Typical optical methods do not allow one to probe these jets at conditions where the injectant temperature, T_{inj}, approaches the critical value, T_{c} (= 282.35 K for C_2H_4). Prior to these measurements, jet droplet sizes were unknown and no feedback could be given to modelers. For this experiment a monochromatic X-ray beam, ~0.1×0.1 mm^2 in size, having a photon flux of ~10^{11} s^{-1} was directed through a C_2H_4 plume from injectors ranging in internal diameter from 0.5 to 1.0 mm. While configurations used were specific to each experimental campaign (for example, different detectors have been used), they are nonetheless fairly similar.

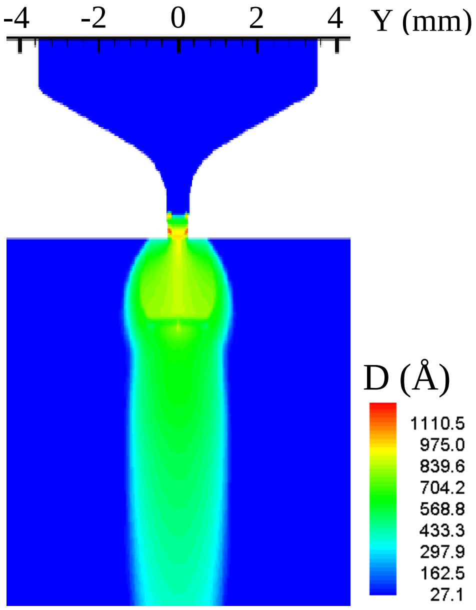

Figure 4: Droplet Diameters from 1-mm-Diameter Injector at T_{inj} = 286 K.

For the measurements described by Figure 3, the C_2H_4 jet was injected into quiescent N_2 at a chamber pressure of 126 kPa; C_2H_4 injection pressures were held approximately constant at 5.15 MPa. A digital 2D array detector, located 3 m from the jet, captured the forward scattered X-ray photons, while a "mask" blocked the direct beam. Diameters of scattered particles then can be derived from the specific radial distribution of scattering. To our knowledge this is the first time that the interior of a condensing, optically thick, supercritical jet has been studied [57]. Typical droplet diameters from this work are 500 to 1000 Angstroms (Å) under these injection conditions, as shown in Figure 3. It should be noted that a range of radial positions was probed; the droplet diameter and volume fraction are seen to decrease with increasing radius at a downstream location of 1 mm from the jet exit. Furthermore, with a scattering calibration, droplet number density and volume fraction can be derived from the absolute scattering intensity. Also, shown in Figure 4 is a preliminary CFD simulation of the droplet diameters from a 1-mm injector (one the injectors used at the APS); this calculation was performed by Prof. J. Edwards, (North Carolina State University). Reasonably good agreement is now obtained between measurements and calculations for droplet diameters; however, model predictions for liquid volume fraction are currently an order of magnitude below the measured values. The reasons for this discrepancy are unknown but will be a focus of future research.

A new effort was begun in 2009, to probe the flowfield within the injector. Thus, a 2D, rectangular-cross-section injector was designed that would allow the integration of diamond windows, so that droplet diameters could be measured inside the injector. In spite of these efforts, it was determined that leaks around the windows may have compromised the measurement of drop sizes. So, in 2010, we began exploring designs of axisymmetric injectors made from beryllium (Be), a material with good X-ray transparency due to its low atomic mass. In 2011 we demonstrated this design by making droplet size measurements within the injector. This, of course, was a very challenging experiment that required discrimination between the droplet scattering from the background scattering from the Be injector. Experimental campaigns were conducted in 2011 and 2012, probing both internal and external flowfields. A sample set of measurements is shown in Figure 5 for an injection pressure of 5.11 MPa and an injection temperature of 286.6 K. This leads to a jet that displays moderate condensation (and is, in fact, not optically dense). The motivation for focusing on this injection temperature (and not a value closer to the critical value) is that the droplet sizes were within the upper detection limit (about 160 nm) for the SAXS instrument as configured for this measurement at the 12-ID-B beamline at the APS. Here a measurement at a location -1.5 mm upstream of the jet exit is shown along with a corresponding measurement 1.4 mm downstream of the exit. It is seen that particle sizes upstream of the exit are extremely small, ~2 nm (= 20 Angstroms) in diameter. Remarkably, it is found that as soon as the jet exits the injector, the particle sizes increase dramatically; at x=1.4 mm downstream of the jet exit, the derived particle sizes are near 100 nm (1000 Angstroms). More details can be found in Ref. 103.

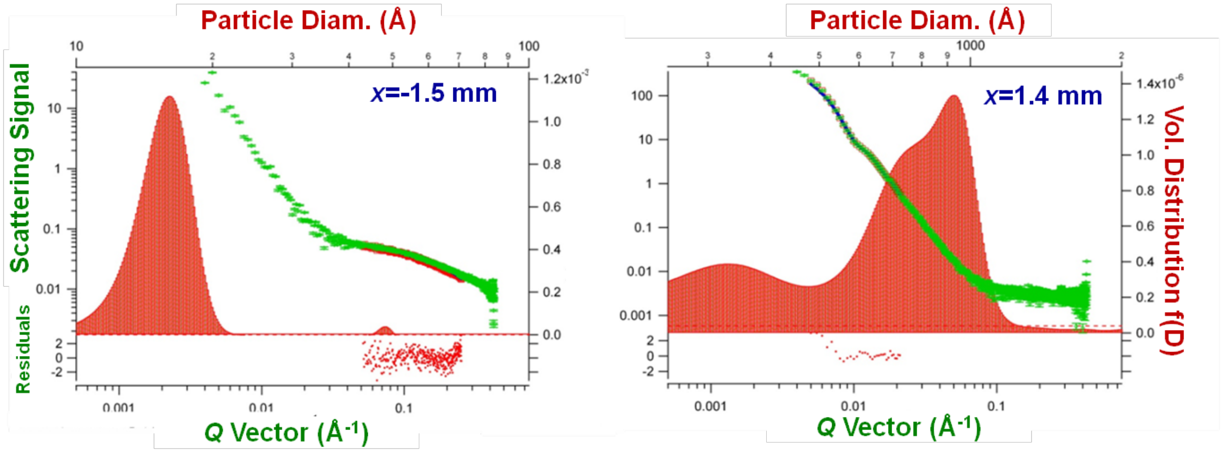

Figure 5: Measurement of Droplet Size Versus Q Vector.

4.1.2 Aerated Fuel Injection

A liquid hydrocarbon is of course an attractive scramjet fuel: it offers high energy density, storability, and critical cooling capability. Over the course of a scramjet flight, the use of liquid fuel as the thermal management medium for the scramjet engine of the entire vehicle will cause the transition of the fuel from liquid to gaseous, supercritical, or two-phase states. At the most basic level, the nature of the fuel plume (whatever its state and composition) and its interaction with the boundary layer and shock structures (including the shock structure that the injectant plume creates) are key elements in designing an effective injection system. Ideally, the fuel injectors/fuel delivery system must *i*) handle two-phase, gaseous, and/or supercritical fuel, *ii*) involve a reasonable number of injection sites, and *iii*) achieve good penetration, good macroscopic scale mixing, or some reasonable combination of the two in a controllable manner and at a reasonable pressure loss. Meeting all of these requirements is of course a challenge. While the fuel is likely to be liquid upon startup of the engine (exacerbating the "cold-start" problem), it is not likely to remain liquid upon injection (after cooling the engine).

As noted above in USAF scramjet flight scenarios, high vehicle heat loads will ensure that the fuel (initially a liquid hydrocarbon such as a JP-7) is vaporized before injection; this provides motivation for studying injection of superheated and supercritical fluid into the sub-critical environment of the combustor. Initially, however, at the critical ignition point, one is left with relatively cold liquid fuel that must be injected into a supersonic crossflow, adequately mixed, and a substantial fraction ignited (by some means) and burned. One approach that has shown much promise for the cold liquid fuel is to use aeration, thereby creating a two-phase fluid; here, gas is added just prior to injection such that a two-phase flow is formed within the injector. Our aerated injector, the so-called *Outside-In* injector design is shown in Figure 6. Upon passage of the two-phase mixture through the injector orifice, the gas expands into the surrounding low-pressure air stream, ensuring a finely atomized spray *still* having very good penetration into the high-speed crossflow. After injection into the high-speed air stream, aerodynamic forces quickly act to further atomize the spray.

Key questions that have guided this research are as follows:

- What are the fundamental processes by which liquid and aerated-liquid jets (with modest gas loading of a few percent) breakup, particularly in high-speed crossflow? Insights obtained from this study can be useful for the design and modeling of liquid injectors, aerated and pure. Furthermore, these fundamental measurements form a basis for judging other advanced approaches.
- Is there an optimum gas-to-liquid ratio (*GLR*, specified on a mass basis) or is more gas always better?
- What is the structure of the aerated gas (annular, well mixed, etc.), and does the gas loading affect the structure
- What is the relationship between the crossflow properties and the jet structures, both in the near and far fields, and how does the plume change during the ignition transient (supersonic to subsonic)?

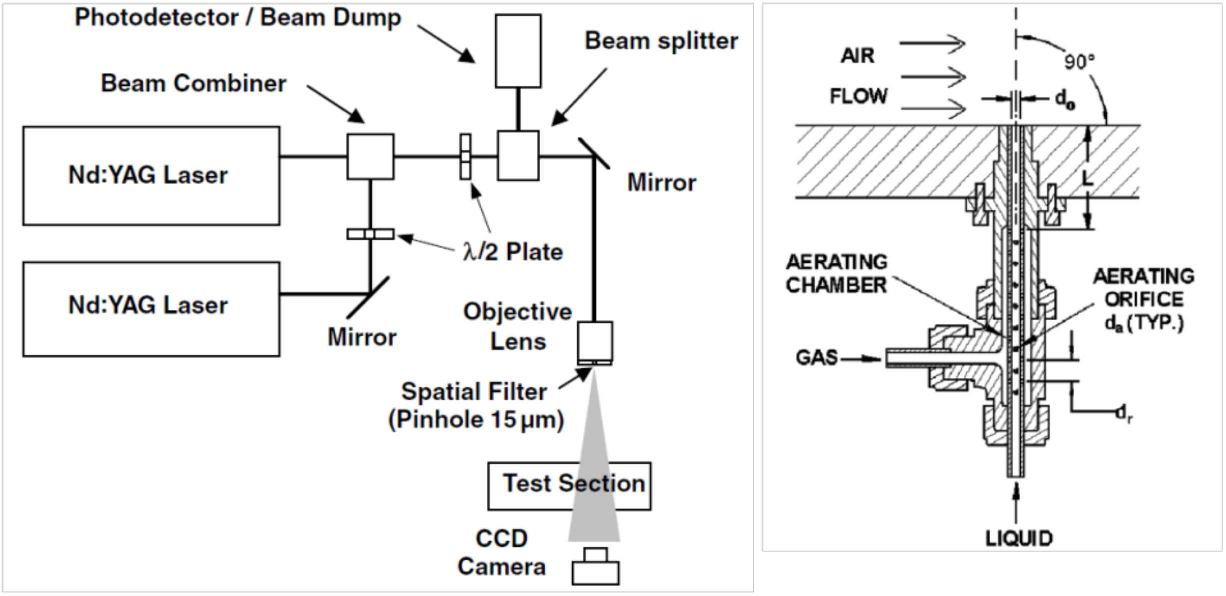

Figure 6: Layout of Digital Holographic Microscope (Left) and Schematic of Outside-In Aerated Injector (Right).

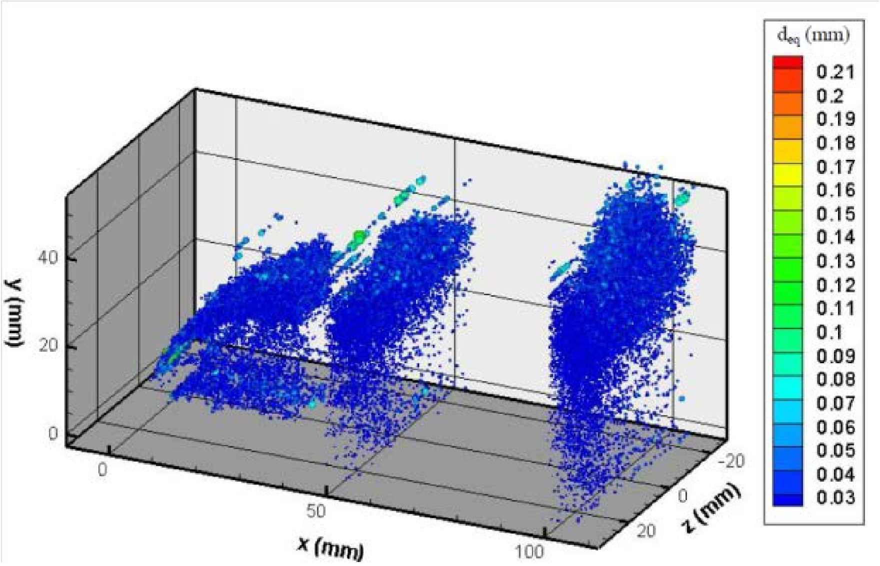

Figure 7: 3D Map of Droplet Sizes [107].

Test Conditions: GLR = 4%, Freestream Mach number = 0.6, Jet Exit Diameter d_0 = 1 mm.

In our original work (also employing holography, but with plates and manual analysis), it was found that downstream in the Mach-2 flow the atomization of the resulting spray is relatively complete at the axial location of $x/d_0 = 100$ (d_0, the injector exit diameter, was 0.5 or 1 mm) and that the *flux-weighted* Sauter mean diameter, $SMD \equiv \Sigma d^3/\Sigma d^2$ (where d is the particle diameter), is roughly constant at 10 μm, regardless of aeration level (including no aeration); this result might be expected due to the strong aerodynamic forces acting on the spray. However, penetration with, say, 5% aeration level is significantly higher than with no aeration, and the area of the plume with drops diameters (SMD) of ≤ 20 μm is nearly twice as large (as that with no aeration) even at x/d_0 of 200. Measurements such as these are critical to understanding the resulting spray and to efforts at modeling these two-phase flows. In both cases (near and far fields), however, measurements are difficult due to the density of droplets.

To study the plume formed by the aerated jet, a digital holography technique has been developed, in collaboration with Prof. K. Sallam (Oklahoma State University). The advantage that holography offers is that, in principle, the entire 3D spray volume can be interrogated, on an instantaneous basis using Q-switched Nd:YAG lasers; however, desired spatial resolution will ultimately limit the region of interrogation. Conventional, plate-based holography is limited too in some important respects: collection and analysis of the plates is extremely time-consuming and the chemicals used for development are hazardous. Thus, effort has been invested in developing a digital approach, wherein the spray is recorded on a digital camera array and droplets and ligaments are then automatically identified (and characteristic length determined). The optical layout for a two-pulse holography setup is shown in Figure 6. Here, a pair of Continuum Surelite Nd:YAG lasers were employed, so that droplet velocities can be derived along with droplet/feature size. The detector was a Redlake EC16000 interline-transfer charge-coupled device (CCD) array with 4872×3248 pixels; of course, this research is aided by the availability of increasingly large digital camera arrays (like this one with 16 million pixels). With the interline-transfer architecture, two images can be recorded on two independent frames, and droplet/ligament velocities can thus be derived. The lasers, optics, and camera were all placed on a large 3-axis translation table, located beneath the windtunnel. This enabled convenient placement of the holography probe anywhere within the spray. The windtunnel employed for this work is located in Research Cell 18 (the so-called transonic tunnel), and freestream Mach numbers of 0.3 and 0.6 were used. The field of view was 5×5 mm^2, while the resolution limit was about 5 μm (based on images from a standard USAF target). This relates to a detection limit for drops of 22 μm (i.e., 4-5 times the resolution limit). Results for this effort are shown in Figure 7 for the case of a water flow rate of 21.3 g/s, a *GLR* of 4%, and an injector orifice size of 1 mm (from the *Outside-In* injector). These measurements show that there are many droplets/features with equivalent diameters of approximately 30 μm (or less, down to the detection limit). It was also found that as the *GLR* increased (from 0 to 8%), the number of large droplets (predominantly on the upper boundary of the jet) decreased, while the penetration increased. At the Mach-0.3 tunnel condition, the influence of the counter-rotating vortex pair was especially evident. This research will be summarized in Refs. 106 and 107.

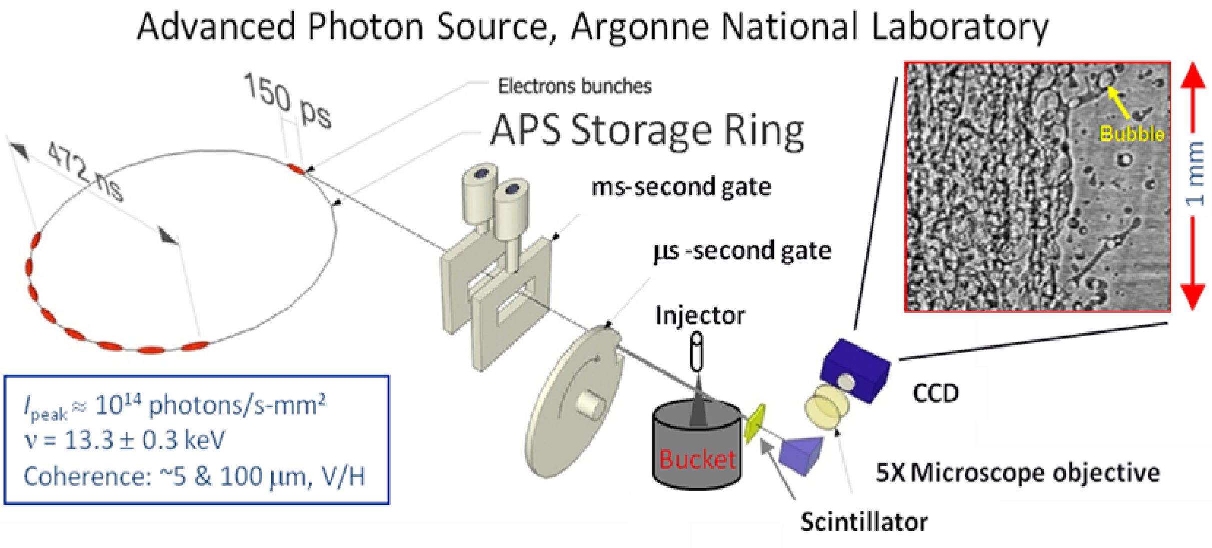

Figure 8: Layout for Phase Contrast Imaging at the Advanced Photon Source (32-ID Beamline) and a Sample Image.

Not only does this approach provide fundamental data for the understanding of liquid sprays, in general, and aerated sprays in particular, but it also provides a database for spray modelers. This is an important point: no other technique currently enables the characterization of spray structures and droplet/ligament velocity *within a volume* on an instantaneous basis. Currently, there is a dearth of spray data of the sort shown in Figure 7, and this effort will thus provide critical data for model development and validation. Nonetheless, it is worth noting that one cannot easily probe the very near field of the injector (within a few injector diameters) where the optical density of the jet is especially high.

To enable the probing of the near field of the injector and, in particular, to probe *inside* the spray, an effort was begun to employ synchrotron radiation to visualize aerated jets at the Advanced Photon Source (APS), Argonne National Laboratory. Here, the line-of-sight techniques of *phase-contrast-imaging* (PCI, in the 32-ID beamline), shown schematically in Figure 8, and radiography (in the 7-BM beamline) have been employed to study the aerated jet issuing into quiescent air. In general, measurements were made with variations in *i*) liquid flow rate, *ii*) gas-to-liquid ratio, *GLR*, and *iii*) nozzle design. For PCI the synchrotron was run in the so-called *bunched* mode with a photon irradiance of 10^{14} photons/s-mm^2, so that high temporal resolution could be attained for each camera exposure: each image represents a 150-ps (1 picosecond = 10^{-12} s) snapshot of the jet; the next isolated X-ray pulse occurs 3.7 μs later, the transit time for electrons within the synchrotron storage ring. Here, the X-ray beam penetrates the jet and then impinges on a scintillator crystal (LYSO:Ce) that converts X-ray radiation to visible radiation; this visible radiation is then imaged by an interline-transfer CCD (PCO Sensicam) with 1280×1024 pixels using a 5× microscope objective; it is noteworthy that the camera can be configured to record two X-ray images (with the time increment, 3.7 μs, corresponding to the round-trip time of the electrons within the synchrotron storage ring), and thus under some conditions, droplet/feature velocities can be derived.

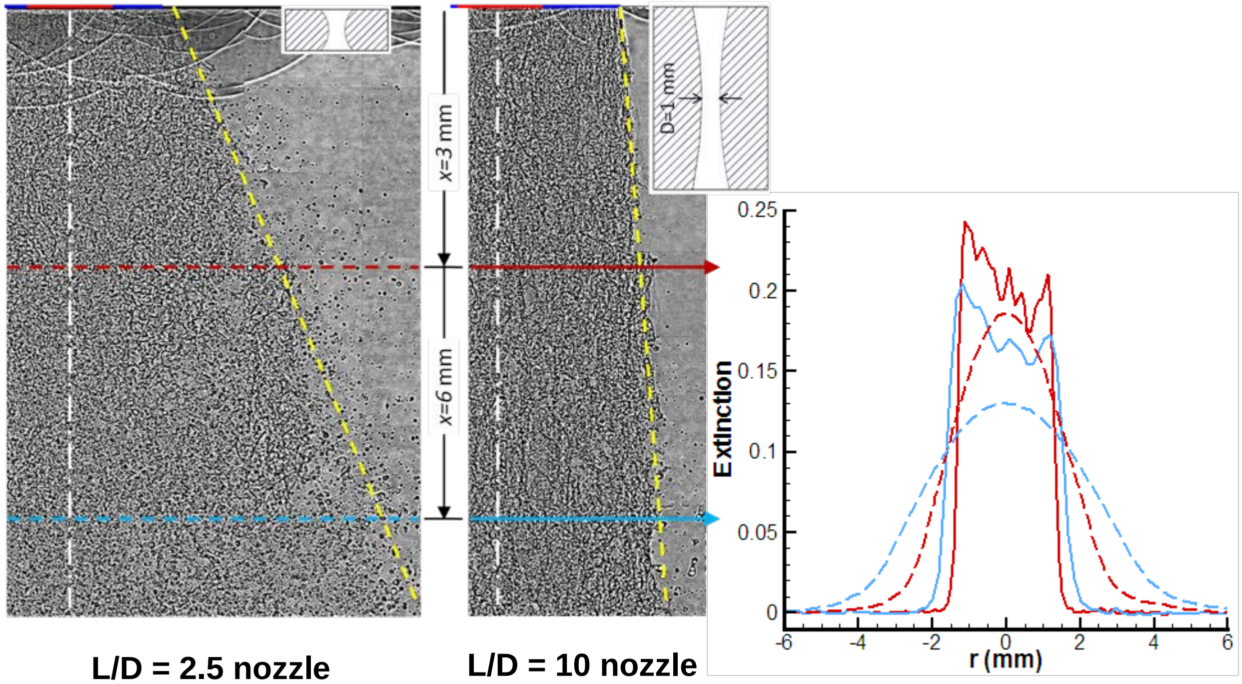

L/D = 2.5 nozzle **L/D = 10 nozzle**

Figure 9: Effect of Nozzle Design (L/D = 2.5 & 10) on Injector Spray Pattern.

Phase Contrast Images (left) and X-ray extinction profiles (below) at y=3 and 6 mm across the jet.
Water $\dot{m}$ *= 18 g/s; GLR = 2%.*

The resulting images (see Figure 9) show for the first time structure <u>within</u> the optically dense part of the aerated liquid jet [80]. Here, two composite images (each image is made up of several instantaneous exposures) show the effect of using two nozzle designs, differing only in their length-to-diameter (*L/D*) ratio. The resulting sprays are remarkably different, however, and it appears that the longer nozzle facilitates expansion of the two-phase fluid (providing a dense, high-speed flow at the exit), whereas the fluid exiting the shorter nozzle experiences strong expansion at the exit (providing a lower-velocity, lower-density spray that has greater lateral spreading). It is believed that the nozzle also affects the mixing field within the injector, through the pressure field.

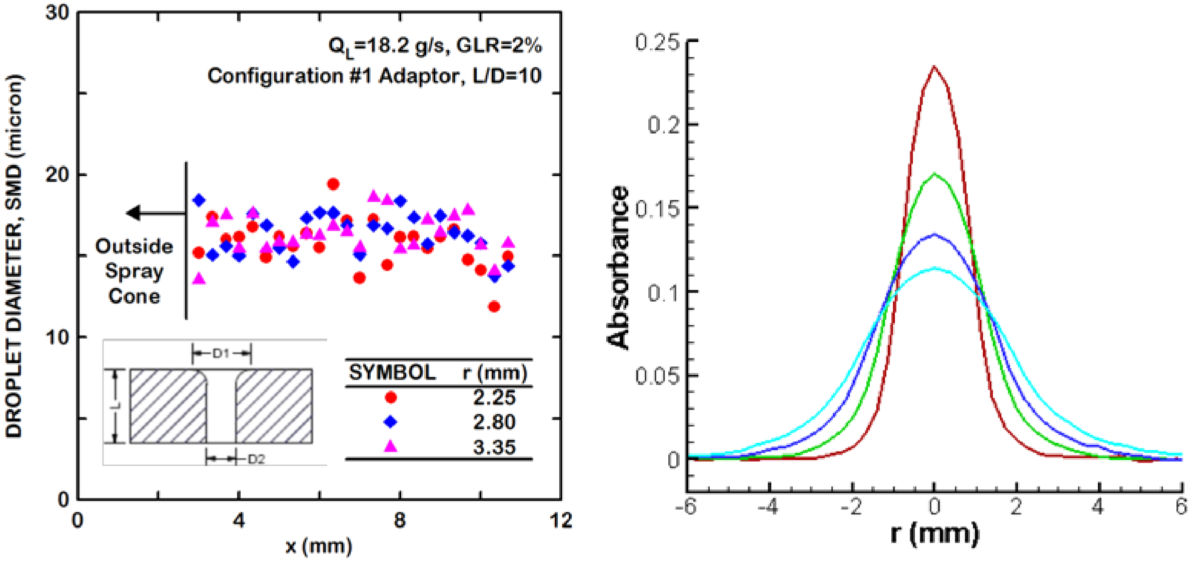

Figure 10: Droplet Size Measurements from Phase Contrast Imaging (Left); Radiography Profiles (Right) at x=1.5, 3.0, 4.5, and 6.0 mm.

Of course, a limitation of this approach is that the field of view is necessarily small, < 2×2 mm^2, due to the small size of the X-ray beam. Nonetheless, these images demonstrate the feasibility and utility of PCI for studying optically, aerated dense sprays. Indeed, one significant advantage over other techniques is that one can potentially distinguish between liquid droplets and bubbles: whereas droplets have darker interior regions (due to X-ray absorption by the water), bubbles have lighter interior regions (but a dark edge, from the water absorption). Indeed, it can be seen in the sample image in Figure 8 that the flowfield is composed of droplets, ligaments and bubbles. While small droplets and bubbles are clearly identified in the low-feature-density region of the spray, the core of the spray may have too many overlapping features to enable identification of individual droplets. Nonetheless, in some regions, toward the perimeter of the spray, sizing of droplets and bubbles can be accomplished, and a Matlab™-based code was thus written to identify and size droplets and bubbles. The code was designed to disregard overlapping features; in general, then, the bubbles tend to be undercounted (particularly larger bubbles, since they have a greater probability of overlapping other features). One such result is shown in Figure 10 (left) for a case with a liquid (water) mass flow of 18 g/s, a *GLR* of 2%, and the specific nozzle adaptor shown. In the near-field under these conditions, the *SMD* for droplets was about 16 μm, while that for bubbles was about 36 μm [82].

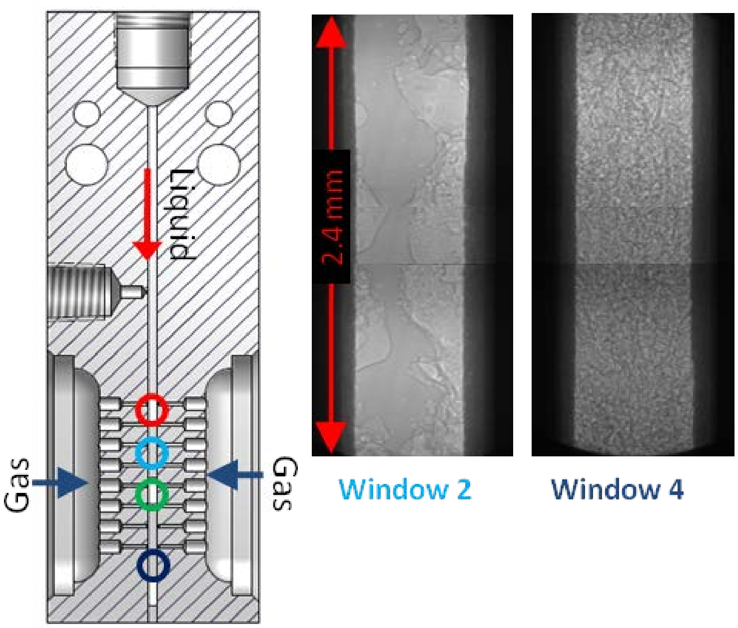

Figure 11: 2D Aerated Injector and Sample Images from Locations 2 and 4.

This technique was also applied to a 2D injector, to aid in our understanding of the flowfield formed within the injector (where the gas mixes with the liquid) [71, 80, 88]. Sample images are shown in Figure 11 for two downstream locations. At the upstream location ("Window 2"), we see the gas, which is fed from the side ports, is mixing with the liquid (fed from the top channel). At the Window 4 location, the gas and liquid appear well mixed with many small features. As noted previously, the line-of-sight nature of these techniques can make interpretation difficult. Nonetheless, these images show with remarkable clarity the rapid mixing of the gas and liquid within the injector (with a high density of interfaces across the column of fluid). Measurements at high *GLR* (8%) show that the mixing of gas and liquid occurs earlier (more upstream) and that scale sizes are smaller at Window 4 (indicating finer scale mixing). Also shown in this study was the effect of the injection pressure (measured at the upstream pressure tap).

Most recently, in 2011, we employed X-ray radiography (wherein one uses an X-ray absorption measurement) to map out the time-average liquid (water) distribution within aerated liquid jets. Here, the spray (into a quiescent environment) was placed in the path of a small X-ray beam using automated translation stages; the photon energy was adjusted to 6 keV to achieve a reasonable extinction of the beam across the spray path (extinction ≈ 0.90/mm of water), and the spray was translated across the X-ray beam path at fixed heights (and then the spray rig was moved to a new height). In Figure 9 are shown the radiography profiles that correspond to the PC images shown on the left. While the jet extinction profiles with the short convergent-divergent nozzle (length-to-diameter ratio L/D=2.5) are smooth and symmetric—as are the radiography profiles shown in Fig. 9 for a 2nd short nozzle design—those with the long nozzle (L/D=10) have very sharp, distinct features that persist as the spray moves downstream. This may be due to imperfections in the nozzle (from fabrication) or to the manner in which the aerating gas is fed into the liquid. The profiles with the long nozzle also imply that there is more water at larger radii. Whether this is because the droplet density is higher at larger *r* or the droplet diameter is larger at larger *r* is not clear, and unfortunately, the high feature density evident with the PC image with the long nozzle prevented droplet sizing measurements.

An interesting conclusion from this work is that it is most likely for an annular-like liquid distribution to exist inside the injector and within the resulting near-field jet at low liquid flow rates, even at high aeration levels. Furthermore, the following was concluded: *i*) the injection condition capable of generating a two-phase mixture with a high gas void fraction within the aerated-liquid injector does not necessarily produce well-dispersed sprays for each adapter configuration; *ii*) it appears that the injection pressure and the gas phase density can greatly affect the structures of aerated-liquid jets; *iii*) the benefit for liquid aeration diminishes as the aeration level reaches a threshold value that decreases as the liquid flow rate increases.

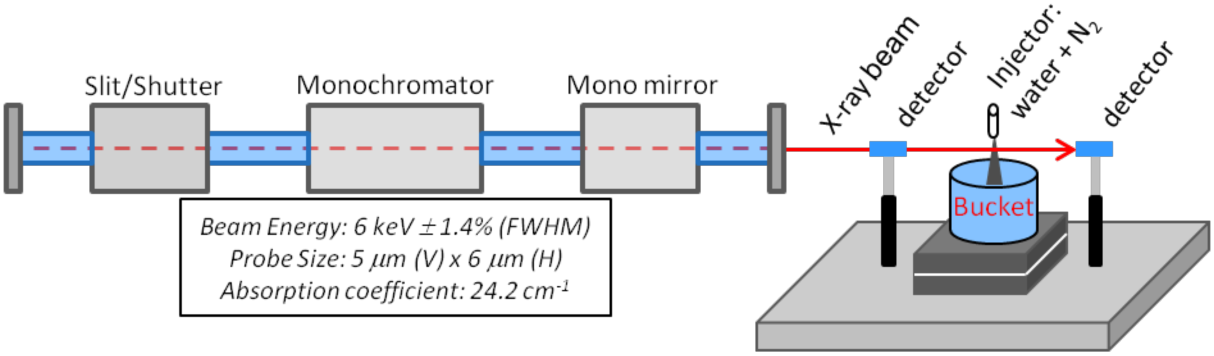

Figure 12: Layout for Radiography at the Advanced Photon Source (7-BM Beamline).

4.1.3 Gaseous Fuel Injection

As noted above our investigation of gaseous fuel injectors has ranged from the study of simple circular wall injectors to the study of more complicated approaches, such as the use of pylon-based injectors [8, 20], tandem injectors (e.g., the cascade injector [21]), and diamond-shaped injectors [32, 33, 52]. In the case of simple circular injectors, a recent effort has focused on providing a validation data set for modelers; this is discussed below in the section on **Multidisciplinary Laser Measurements**. Regarding minimally intrusive approaches, Figure 13 shows a diagram of a μ-pylon injector along with an image of fuel-air equivalence ratio derived from vibrational Raman scattering (the approach is described in Sect. 4.3). Injection from the μ-pylon was compared to that from a simple circular injector, and the effectiveness of the μ-pylon was shown in lifting the plume from the floor of the tunnel while providing virtually no pressure loss.

The potential for flush-wall diamond-shaped injectors to improve fuel penetration/mixing and to act as flameholders has been studied also. This work was motivated by the observation that the diamond-shaped injector produces a lateral counter-rotating vortex pair (LCVP) wherein the residence time may be sufficient for flameholding; the overall goals for this effort were to *i*) characterize the near-field flow structures and mixing of a diamond-shaped injector, in comparison to that of a circular injector, in a Mach-2 crossflow, and *ii*) investigate the interaction of the diamond jet with small circular *tandem* upstream/downstream jet(s). For a follow-on study, the scope was broadened based on the observation that the tandem jet can be used to

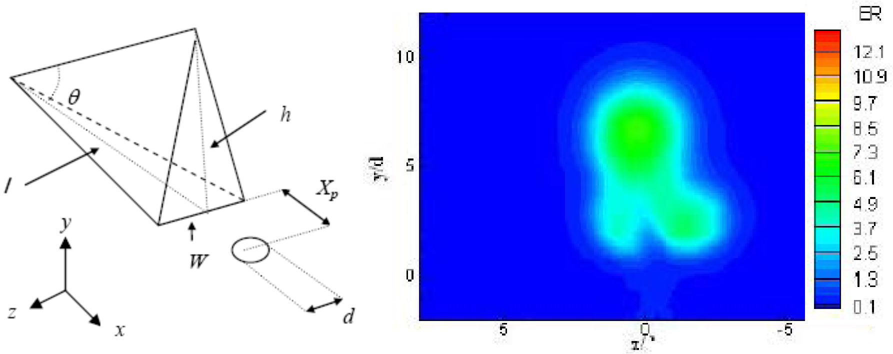

Figure 13: μ-Pylon Injector Schematic (Left) and Spanwise Equivalence Ratio Image from Raman Scattering (Right) for Pylon with h = 6.3, W = 2.5, l = 11, and d = 1.6 mm.

The downstream x/d probe location was 12, while the momentum flux ratio was 4.

control the penetration of the main (diamond) jet, while the injector blocks were redesigned (see Figure 14 vs. Figure 15) to minimize the disturbance of the LVCP by the upstream circular injector(s). For the design shown in Figure 14, the purpose of the upstream jets is to provide hot gas and radicals, from a C_2H_4-O_2 torch, to hold a flame in the LVCP region.

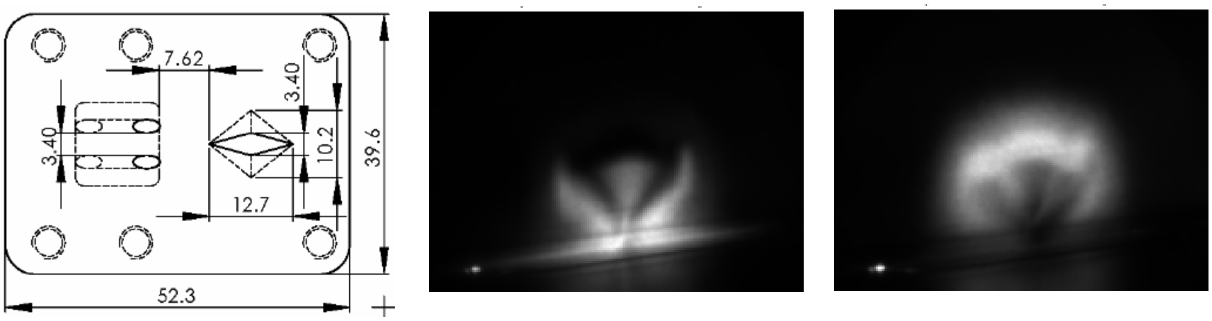

Figure 14: Injector Block (left) and Spanwise NO PLIF Images of Plumes 7.6 mm Downstream (Right) of Diamond Port Center.

Left plume: air from upstream circular ports seeded with NO. Right plume: air from diamond port seeded with NO. Field of view is 70 mm (wide) by 37 mm (high).

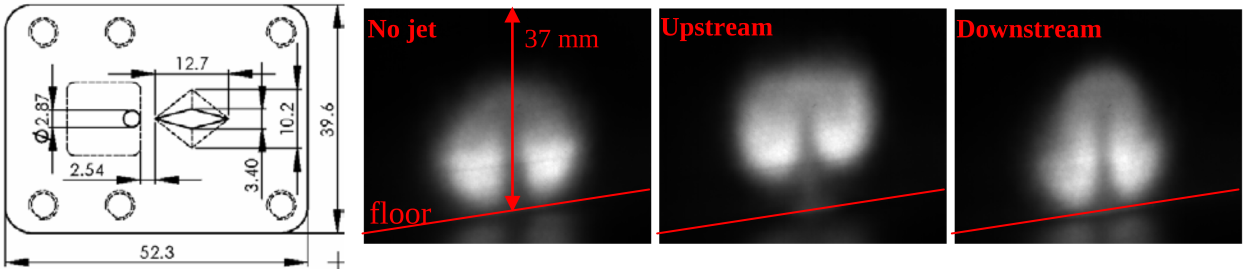

Figure 15: Spanwise NO PLIF Images 45 mm Downstream of Diamond Port Using Single Tandem Jet (left) as a Control Jet.

Injection block orientation was rotated 180° to place tandem jet downstream of diamond port.

To characterize mixing NO PLIF (planar laser-induced fluorescence) was used: NO-laden air (X_{NO} < 500 parts per million) was injected through either the diamond port or the upstream tandem *igniter* ports. Sample frame-averaged NO PLIF images are shown in Figures 14 and 15 (images have not been corrected for perspective distortion). Unfortunately, our attempts to use the LVCP to hold flame were not successful. It is believed that this approach would benefit from higher total temperatures that accompany higher flight Mach numbers, whereas Research Cell 19, as currently configured, is limited to total temperature of about 600 K.

In Figure 15 the influence of the tandem jet on the main jet penetration is clearly shown: if the tandem jet is upstream of the main jet, the entire plume is raised from the floor, whereas if the tandem jet is downstream, the plume appears stretched vertically. Note that this work was in collaboration with Prof. R. Bowersox (Texas A&M University) and Dr. K. Kobayashi (Japanese Aerospace Exploration Agency, JAXA).

4.2 Ignition, Flameholding, and Flame Propagation in Supersonic Flows

4.2.1 Plasma-Assisted Ignition and Flameholding

Key questions that have guided this research are as follows:

- Can one take advantage of non-equilibrium effects within plasma to improve fuel-air reactivity (i.e., enhanced flame and/or ignition chemistry)?
- What are the fundamental physics with a particular discharge? Assuming radicals and ions are produced, what are their roles in enhancing the fuel-air reactivity?
- Can one leverage a modest power/energy to generate the plasma to affect the flowfield (e.g., initiate fuel-air combustion, enhance flameholding (e.g., stabilize a rich mixture), and/or generate shocks that affect the flowfield beneficially (e.g., trip the boundary layer)?

We have focused on studying fundamentals of plasma-assisted combustion and plasma interactions with a high-speed flowfield, and an outgrowth of this work has been the development of compact, efficient pulsed plasma power supplies and plasma igniters. In our studies of plasma-assisted combustion, advanced diagnostic tools have been used to elucidate underlying physics for the effectiveness of various schemes. This is shown in our collaborative efforts with Prof. Y. Ju (Princeton University, see Ref. 13) and with Profs. M. Gundersen and H. Wang (University of Southern California, USC, see Ref. 34). In both cases advanced diagnostics have led to a new understanding of the role of plasma on combustion. For example, in the work

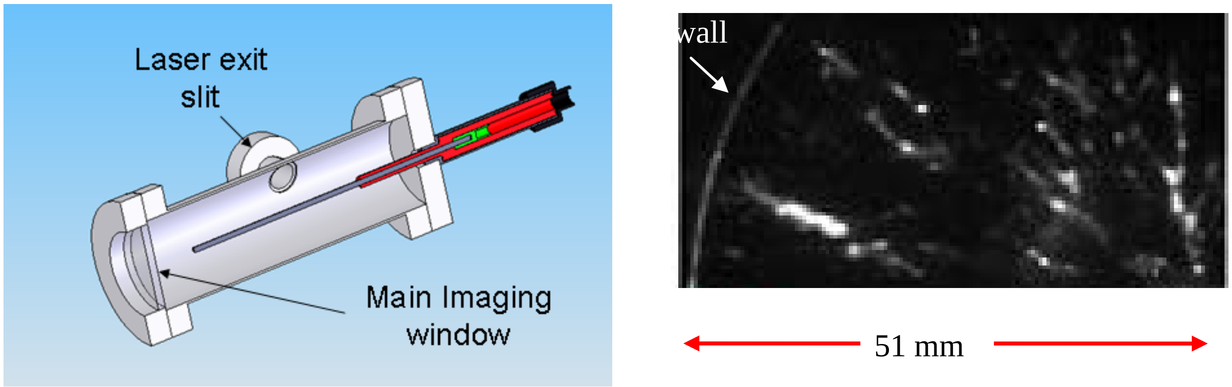

Figure 16: Chamber (Top) and OH Across the Top-Left Quadrant from Initial Streamer Distribution 500 ns After High-Voltage Pulse.

with Profs. Gundersen and Wang, a *transient plasma* discharge (60-kV peak, 70-ns duration, full width at half-maximum height) was used to initiate combustion of a quiescent, stoichiometric mixture of methane (CH_4) and air within a chamber (Figure 16, left). For this work PLIF was used to quantify hydroxyl (OH) production within the reactants while high-speed chemiluminescence imaging (2000 frames/s) was used to study flame initiation and propagation. Regarding OH production, Figure 16 (right) shows a PLIF image recorded 500 ns after discharge initiation; "streaks" in the image represent OH created from the initial "streamer" field (in the laser-sheet plane); OH concentrations are estimated to be as high as 10^{15} cm^{-3}. This study showed for the first time, to our knowledge, how the transient plasma initiates and enhances combustion (e.g., decreases the net time for combustion completion) and that while the transient plasma does indeed produce radicals such as OH, combustion always initiates at the central electrode (anode) and not within the bulk gas as initially believed. The flame then propagates outward to the wall (here, the cathode) at a speed consistent with literature values of flame propagation on average, thus demonstrating that species produced by the plasma did not enhance flame propagation in this case, but, presumably, aided in the initiation of combustion along the anode. It is noted that recent measurements have presented some evidence of enhanced flame speed along the streamer path, whereas our observation pertained to the average flame propagation speed. Nonetheless, both high-speed emission and OH PLIF measurements show that combustion initiation is reasonably uniform along the entire length and perimeter of the anode. This, of course, is the reason that previously reported measurements show reduced ignition delay and times to peak pressure, as compared to ignition via a spark plug.

More recent measurements with the USC group have focused on addressing the role of humidity on ignition using the transient plasma. This work was motivated by observations of reduced detonation wavespeed in a pulsed detonation combustor with humid air. Our measurements showed that increased humidity resulted in increased concentration of OH and

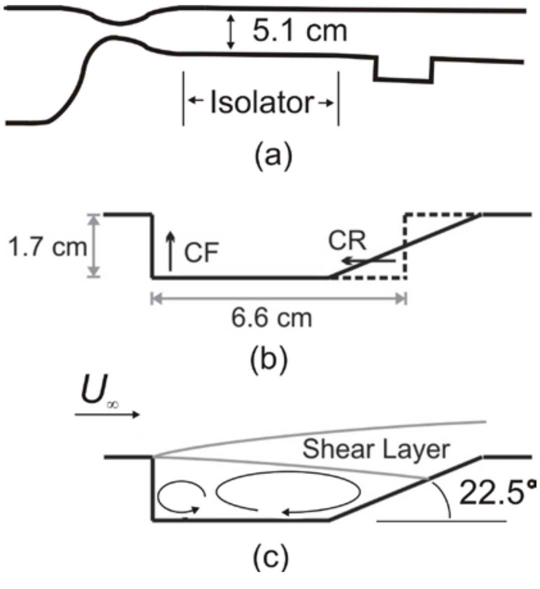

Figure 17: Scramjet Flowpath (a) Showing Cavity with Rectangular and Ramped Close-Out Faces [1].

Shown are flowpath schematic (a), potential cavity fueling schemes (b), and flowfield features (c).

decreased concentration of O_3. This is indicative of the consumption of O atoms (reacting with H_2O). O atoms have been shown to play a key role in combustion ignition; furthermore, O_3 has been shown to increase the laminar flamespeed. Most recently, we have collaborated with groups at USC and The Ohio State University (with Profs. W. Lempert and I. Adamovich) to conduct both thermometry and O-atom concentrations measurements within the transient plasma afterglow. Thermometry was accomplished with the coherent anti-Stokes Raman scattering (CARS) technique in a point-to-plane discharge geometry over a flow of fuel and air (the "plane" was a sintered bronze disk that provided the flow of premixed gases). The probe region was located adjacent to the high-voltage anode (within 250 μm), and here we observed elevated temperatures in this near field region, with values of ≥ 1000 K, depending on the fuel. This observation provides good evidence that the transient plasma creates hot regions with high concentrations of atoms and radicals near the electrode that appear capable of initiating combustion.

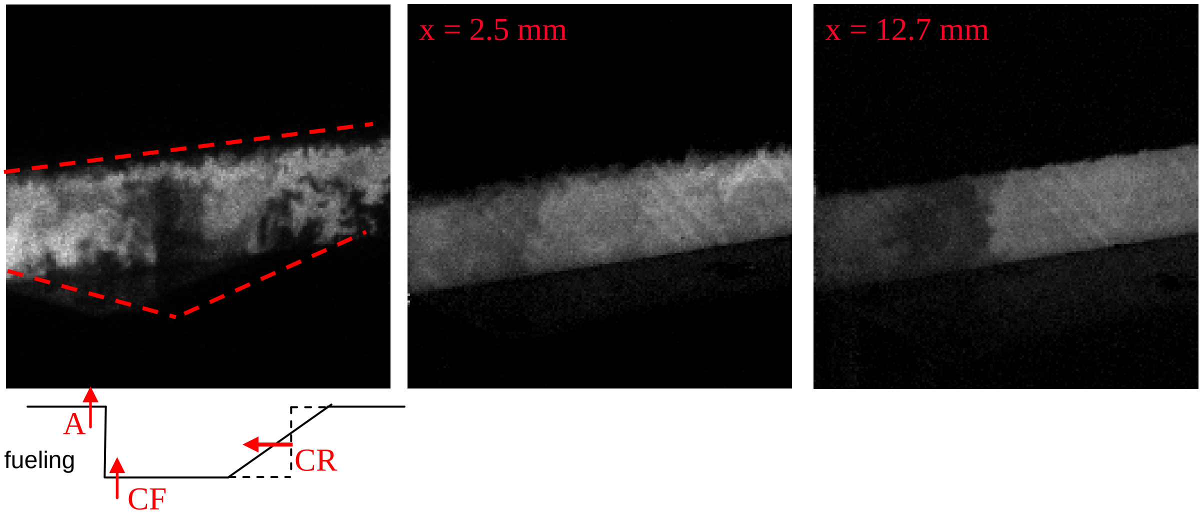

Figure 18: Instantaneous Spanwise PLIF Images.

Left: OH (half-span image, with cavity outline shown in red dashed lines) with cavity flame in a Mach-2 crossflow. Fueling sites are indicated in the schematic above. Center and Right: distribution of injectant (site c) using NO PLIF from two downstream locations.

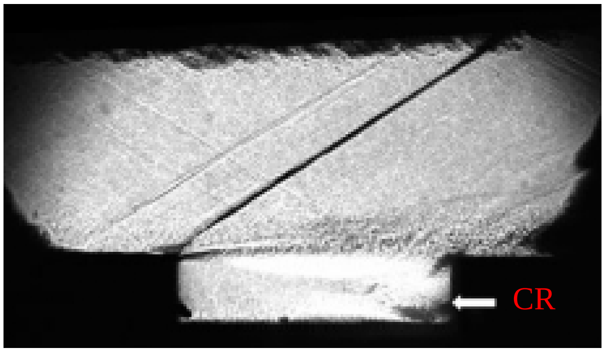

Figure 19: Shadowgraph and Combustion Emission from Cavity with Rectangular Closeout [2].

4.2.2 Flame Holding and Flame Spreading

One key issue facing the design of a flameholder for hydrocarbon-fueled scramjets is the changing character of the flowfield that must be tolerated to ensure wide operability. Prior to ignition, the combustor flow is primarily supersonic. Assuming ignition takes place at a relatively low flight Mach number, the combustor operation is now dual-mode in character: a system of shock waves creates a distorted flowfield containing regions of both supersonic and subsonic flow (as well as separated boundary layer). As the vehicle accelerates, the shock-train weakens, and the flowfield returns to mainly supersonic. Clearly, a robust flameholder must continually capture a small portion of the high-speed core flow, establish a stable combustible mixture, and hold the main-duct flame by providing a source of heat and radicals and do all of this without excessive drag penalty.

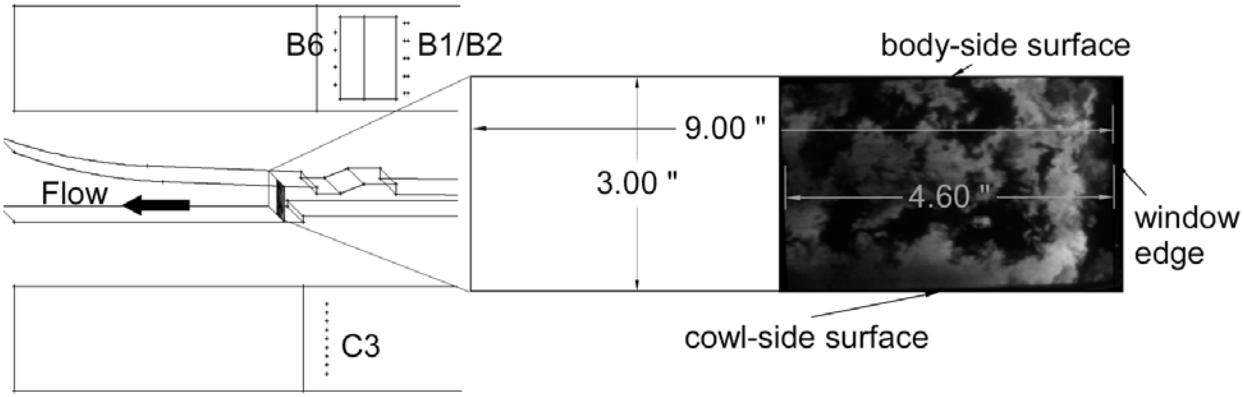

Figure 20: Schematic of Scramjet Combustor Showing Location of OH PLIF Interrogation Plane [51].

In this program, a wall cavity has been the primary focus of research for flameholding and flamespreading (though as noted above, in relation to the diamond injector, novel approaches have been studied too). Within this wall cavity, shown schematically in Figure 17, local stoichiometry appears to vary in all three spatial dimensions, although in general the overall mixture is often rich, due to the abundance of fuel adjacent to the wall. Some information on both the temporal and spatial behavior has been captured with OH planar laser-induced fluorescence measurements (Figure 18, left-hand image, 19 mm from the leading edge). The spatial dependence of the mean flame location depends on fueling scheme, overall equivalence ratio within the cavity, and core-flow conditions, particularly those that affect the shear layer. Our research shows that direct fueling, for example via the cavity closeout face (ramp or rectangular), site *CR* (Figure 17), allows for a broader range of cavity-flame operability (lean and rich blowout), although the best performance, in terms of heat release and stability of operation is probably attained when both fuel and air are added to directly to the cavity.

It is also interesting to note that while site *CF* is also within the cavity, the resulting fuel jets tend to interact strongly with the shear layer, again making the cavity flame especially sensitive to shear-layer perturbations. Three observations are worth noting: *i*) a cavity/core-flow shear layer flame is prominent, especially at intermediate fueling levels; *ii*) the upstream corner of the cavity flame appears important for flameholding; and *iii*) at high fueling levels, most of the burning occurs at downstream locations (not in the upstream portion of the cavity). It is also worth noting that while the cavity <u>is not</u> a perfectly stirred reactor, the fuel is reasonably well mixed near the leading edge of the cavity with close-out (*CR*) injection, as is shown in Figure 18 (center and right-hand images), with single-shot NO PLIF. Indeed, the "patchy" flame apparently results from the locally rich mixture (and hence the presence of the shear-layer flame) in the central cavity span. One interesting aspect is that the use of a rectangular cavity—where acoustic forcing of the shear layer is stronger than with a ramped-cavity—does not adversely affect cavity stability in Mach-2 or 3 crossflows, as shown in Figure 19 [1-2].

More recently, a study was conducted in our 1X scale scramjet duct (in Research Cell 22) on flame spreading in a rectangular duct using gaseous fuels. In this design, shown in Figure 20, rearward facing steps are included on both the cowl-side and body-side surfaces, both downstream of the cavity flameholder. It was shown by various measurements, including OH PLIF, that these steps are effective in spreading flame from the cavity-side surface (body side) to the cowl side [51], as shown with the OH PLIF image in Figure 20. Indeed, flameholding and flamespreading were so effective in this configuration that performance was good even with CH_4 fueling.

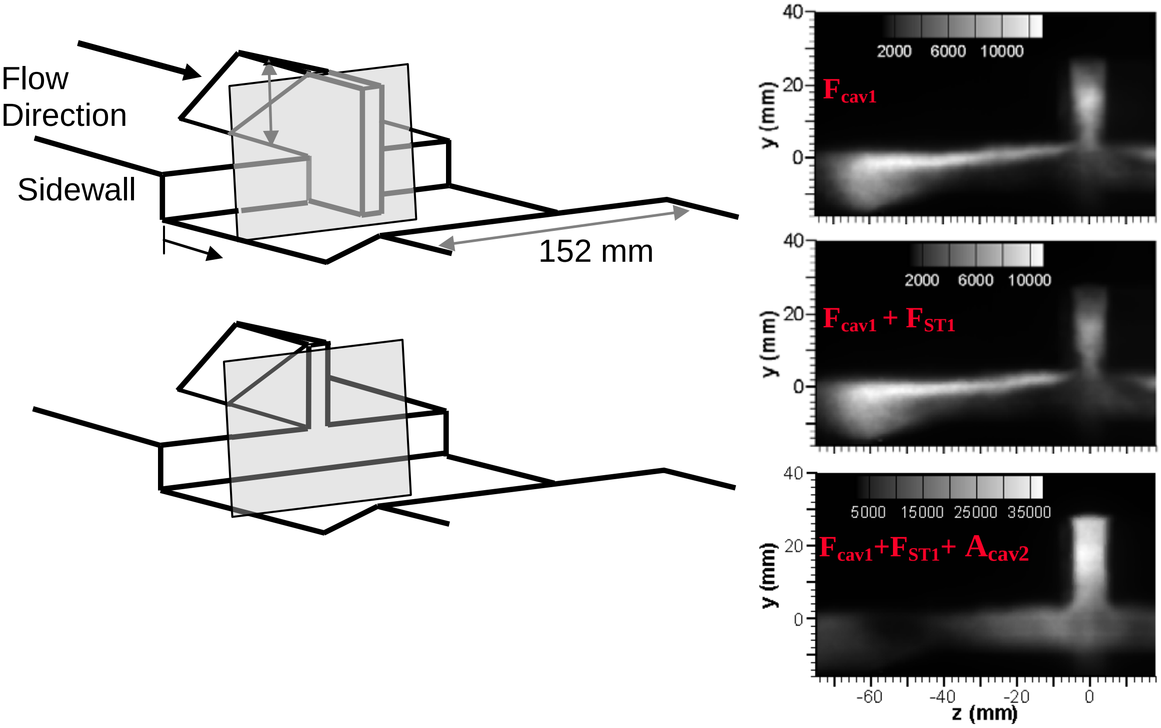

Figure 21: Results from a Study of the Interaction of a Strut and Cavity.

Above: strut-cavity configurations and the PLIF interrogation plane (shown in grey). Right: corresponding frame-averaged OH distributions for the top configuration with fueling from the cavity ramp (F_{cav1}) and/or the strut face (F_{ST1}). A_{cav2} indicates air addition from the ramp face.

Integration of narrow struts with the cavity flameholder has been the subject of a more recent study. This is seen as a good method to both fuel the interior of a larger-scale round scramjet and as a method for propagating the flame from the flameholder to the core region. An example is shown in Figure 21 with 2 sample designs of a strut integrated with a cavity [60]. The interaction between the cavity and the struts, specifically with regard to shock/boundary-layer interactions, makes this a very complex flowfield. To examine the efficacy of these designs, OH PLIF was employed to characterize burning patterns and the degree of reaction taking place. It is

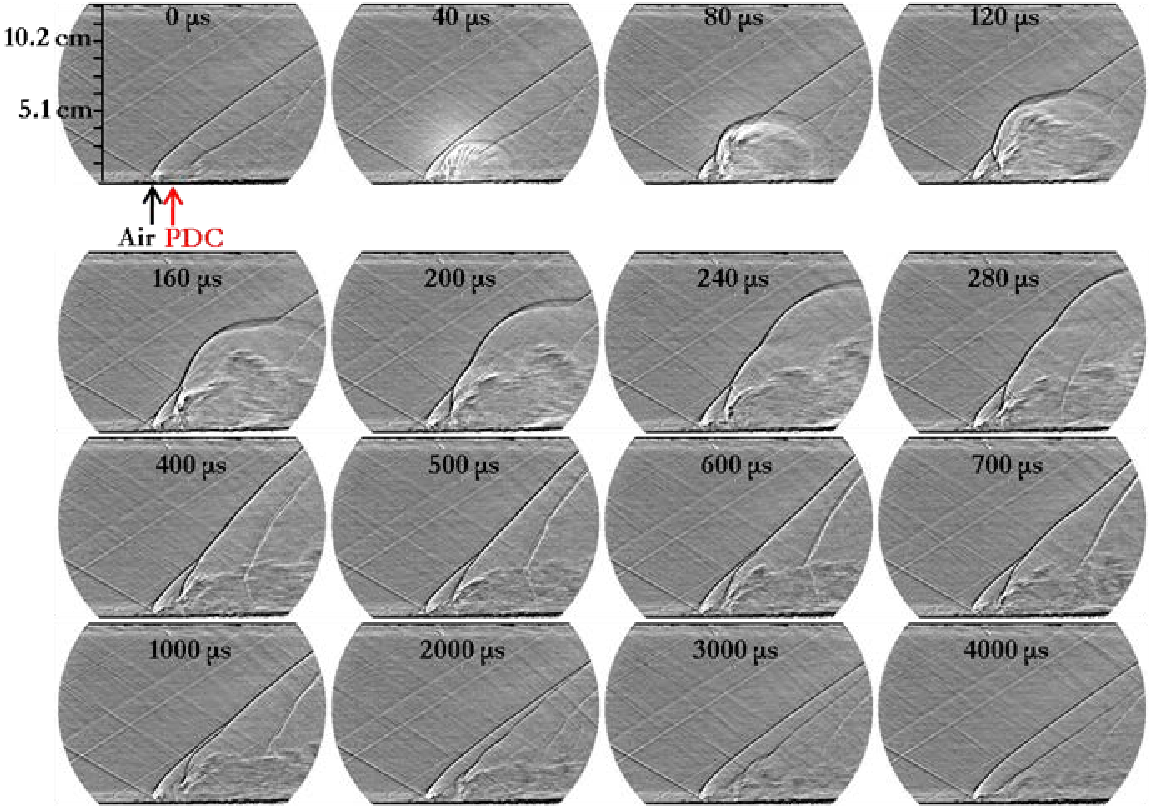

Figure 22: High Frequency (50 kHz) Shadowgraph of PD Plume with Air Injection 2.5 cm Upstream in a Mach-2 Crossflow (Left to Right) [100].

noted that hydroxyl flowtagging velocimetry (HTV) has also been employed to better understand the nonreacting strut-cavity flowfield [104].

The three frame-average images of relative OH concentration in Figure 21 show different fueling options: *i*) from the cavity ramp (top); *ii*) from the ramp and the strut side faces (middle); and *iii*) from the ramp and strut faces and addition of cavity air (bottom). Cavity air addition makes a substantial difference in the extent of reaction, simply because the cavity is otherwise rich (note for example the shear-layer flame that forms at the cavity/shear-layer interface). Note that while the strut is effective in transporting reactants from the cavity, thus spreading the flame, it has been observed that some strut configurations can disrupt flameholding by reducing the fuel-air residence time within the cavity.

In 2010 we began a study with the Pulse Detonation Group (AFRL/RQTC) on the interaction of a pulse-detonator (PD) and a high-speed crossflow [89, 100]. These measurements were carried out in Research Cell 19, in a Mach-2 crossflow, in the 130 ×152 mm^2 tunnel with a secondary jet, placed either upstream or downstream of the PD exit. The PD was installed in one of the removable floor blocks of the tunnel test section. The exhaust of the PD was normal to the flow in the test section. The interaction, which lasts for only a few milliseconds, was visualized with high-speed shadowgraphy (at 50,000 frames per second) and with planar laser-induced fluorescence of nitric oxide (NO PLIF). Propane (C_3H_8) and nitrous-oxide (N_2O) were used as the fuel and oxidizer, respectively, and were chosen because of their reliability of igniting and transitioning to detonation under conditions of low tunnel pressure. Cross-planes of NO PLIF images show the development of the PD jet with and without the secondary jet. Plume images show the counter-rotating vortex pair structure (typical of a jet in crossflow), and therefore the potential for significantly enhanced mixing with the core flow. The interaction of the PD exhaust plume with upstream injection showed enhanced penetration and mixing. Upstream injection at 2.5 and 3.8 cm showed that the plume interaction produced large fluctuations and vortex shedding, leading to more penetration and mixing with the core flow, and a sample set of shadowgraph images is shown in Figure 22. The differences in the PD plume with different upstream injection locations indicated that there may be an optimal distance between the two for maximum mixing and penetration. Furthermore, high-speed wall pressure measurements confirmed the observation of a longer PD blow-down times with continuous upstream secondary injection. Detailed numerical simulations were performed with a simple model of the pressure, temperature, and velocity conditions present in the PD. The model accurately captured the overall PD plume structure through comparisons with the high-speed shadowgraph and NO PLIF experiments, and thus the model can be used in future studies to perform parametric studies of other PD locations and conditions for enhanced mixing.

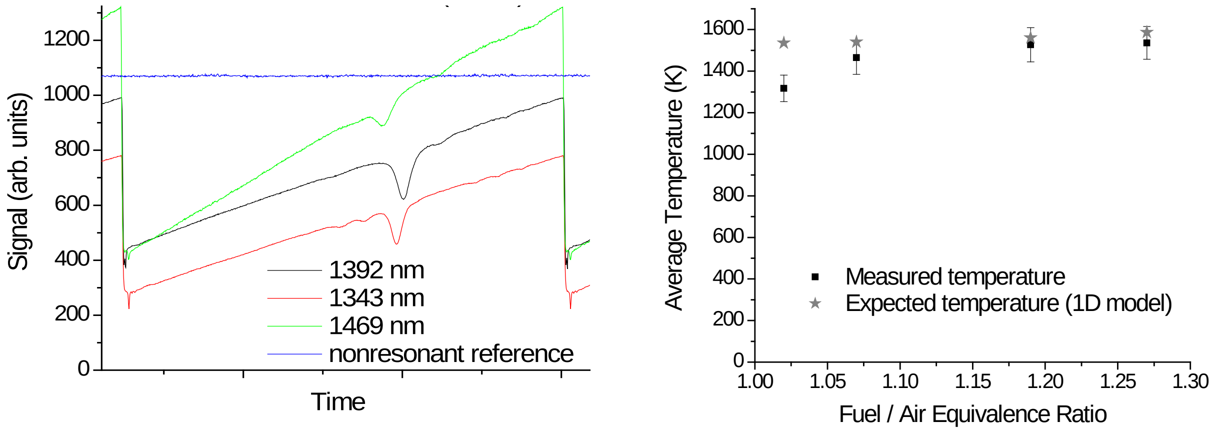

Figure 23: TDLAS Measurements Downstream in Scramjet Combustor, Simulating a Mach-4.5 Flight Condition.

Left, single 4-kHz sweep; right, T versus overall Equivalence Ratio.

4.3 Multidisciplinary Laser Measurements

A particular focus of this program has been on the development and application of advanced optical diagnostic tools for the study of phenomena related to high-speed reacting flows. In general, these techniques are a principal means by which research topics are addressed. Examples of this effort include the application of PLIF—both NO for mixing characterization and OH for combustion assessment—spontaneous Raman scattering, hydroxyl tagging velocimetry, X-ray based techniques such as SAXS and phase-contrast imaging, pressure sensitive paint, and tunable diode laser absorption spectroscopy (TDLAS). Regarding TDLAS, much of the initial effort was in collaboration with Prof. R. Hanson and Dr. J. Jeffries (Stanford University), and good progress has been made over the course of this program to develop a useful diagnostic [6, 29, 42]. Indeed, studies have shown that path-averaged combustor temperature and H_2O concentration can be determined from spectra with low noise content (in spite flowfield turbulence and other “real world” effects) and that TDLAS can, in principle, be used as a controls sensor. A sample set of measurements is shown in Figure 23 from combustion measurements carried out in Research Cell 22. Subsequently, an effort to use CFD computations of the scramjet flowpath to derive synthetic TDLAS temperatures and water vapor concentrations was undertaken [39]. In this way one can more easily compare CFD and experimental measurements. Here, it was shown that the difference between computed line-of-sight-averaged temperatures and synthetic TDLAS temperatures, at least in this instance, was relatively small.

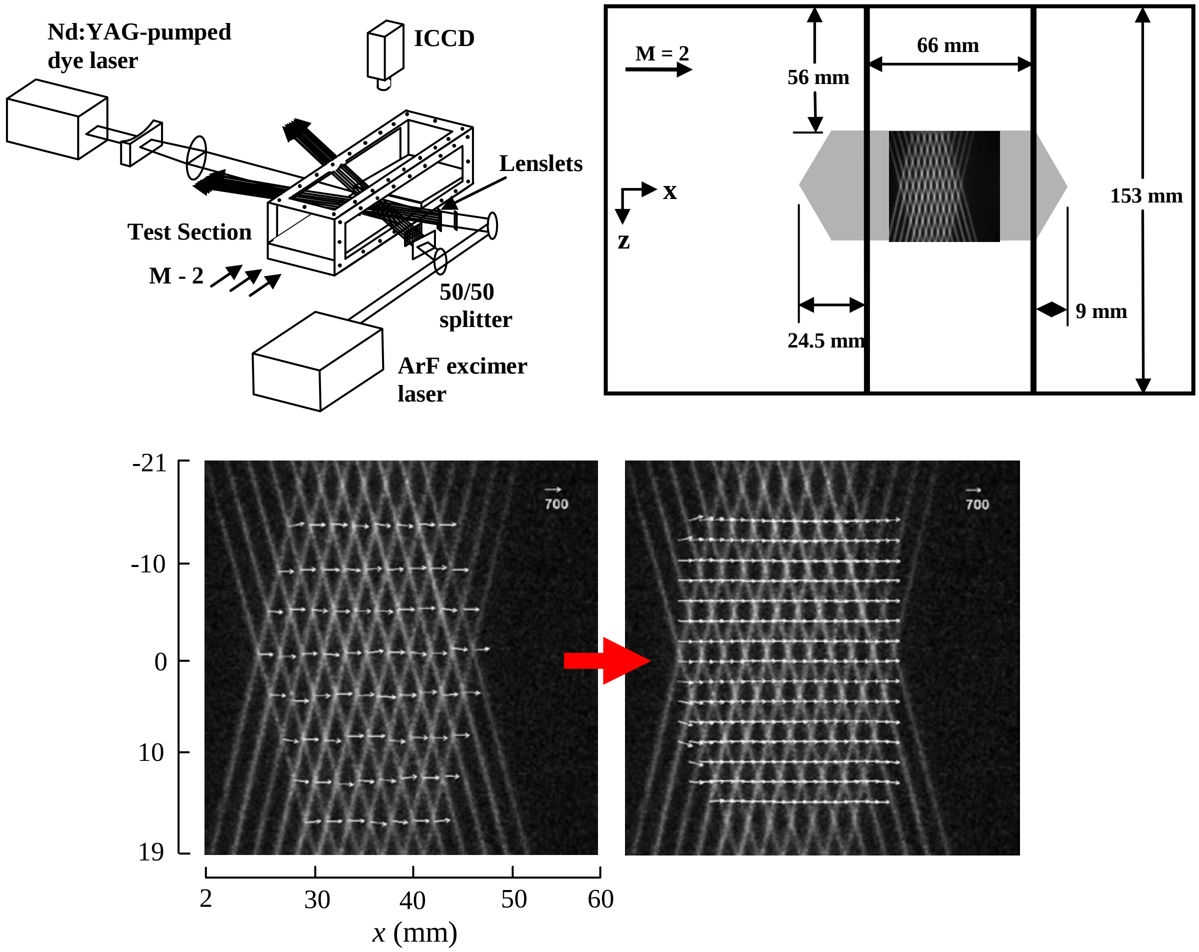

Figure 24: HTV Layout to Probe Mach-2 Flow over a Cavity (Top) and Sample Measurements (Bottom) [67].

Gray region in top right figure represents measurement domain.

A focus for diagnostics development has been on hydroxyl tagging velocimetry (HTV), in collaboration with Prof. R. Pitz, Vanderbilt University [4, 16, 17, 67, 104]. Here, an Argon-Fluoride excimer laser beam (193 nm) is formed into a grid of beams (Figure 24). The 193-nm radiation photo-dissociates water vapor to create H+OH; thus, if OH is probed at a later time—using PLIF—two velocity components can be obtained from the grid displacement (and potentially the out-of-plane component through a stereo measurement). The advantage of a “molecular tag” is that the tagged gas molecules follow the flow with perfect fidelity (while particles cannot). While our first effort, described in Refs. 4 and 16 employed optics to form a 7×7 grid, a follow-on effort employed optics for an 11×11 grid [67, 104]. Nearly the entire set of crossing points was then imaged, as shown in Figure 22. Here, the left-hand figure shows velocities derived from the irregular grid of crossing points while the right-hand figure shows the regular grid with interpolated velocities. A comprehensive velocity map in and around the cavity within a Mach-2 freestream was thus obtained.

Velocities ranged from V = 680 m/s in the freestream to -100 m/s within the cavity. Furthermore, because the read step is based on OH A-X(1,0)/(1,1) excitation/detection—of the overlapped $Q_1(1)+R_2(3)$ line—rejection of laser scattering is good and near-wall regions can thus be probed. RMS (root mean square) values result from a combination of turbulence, determination of the crossing point (e.g., ±0.1 pixel for OH signal-to-noise, SNR=10), and timing jitter between the two lasers (±8.5 ns); indeed, instrumental RMS values were small—contributing as little as ±10 m/s uncertainty to freestream velocities—in spite of the small 193-nm energy per individual beam, ~1 mJ. Some issues, however, remain: grid signal strength within a reacting cavity flow, where there is abundant H_2O, is very weak, while OH grid signal strength within an ordinary hand-held torch is well above nascent OH levels from the flame. This appears to indicate that beam absorption (probably from the C_2H_4) is a limiting factor. Ideally, too, the laser is designed to operate narrowband, so that absorption by the ambient O_2 is mitigated through wavelength tuning, but narrowband operation was not achieved in our work (due to some optical damage within the laser). More recent HTV measurements (using a blend of hydrogen, H_2, and methane, CH_4) have shown that employing flowtagging within the flamezone is still problematic: "pattern noise" arising from the distribution OH within the flamefront makes identification of a grid pattern challenging. Nonetheless, we have demonstrated HTV in the cavity-strut flowfield and have compared the derived velocity field with that derived from large-eddy simulation (LES) [104].

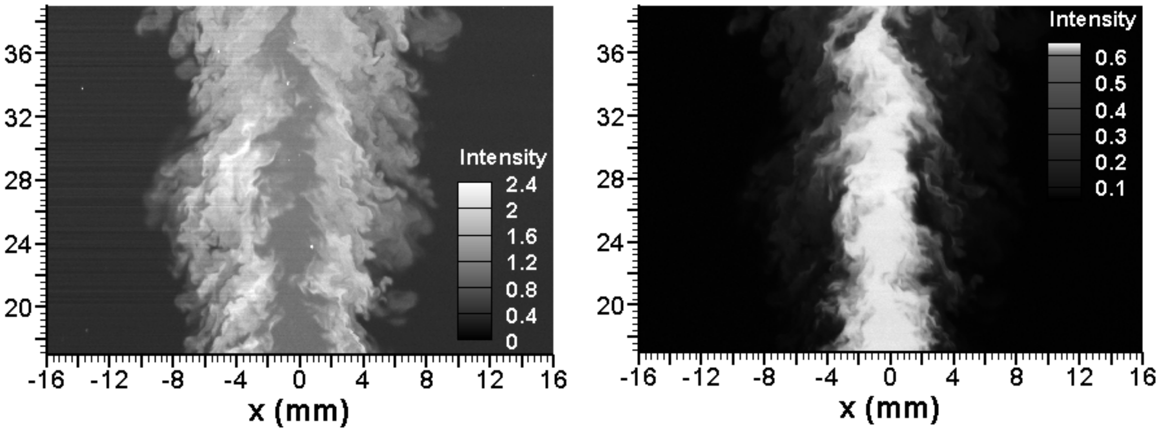

Figure 25: Rayleigh Scattering (Left) and Acetone PLIF (Right) from a Three-StreamTurbulent Jet Flowfield.

Intensity scaling is relative to that from the device for obtaining flat intensity fields.

Our emphasis on diagnostics has also led to an effort to create benchmark data sets for improved fluid-dynamic modeling. A second ongoing effort, to improve LES mixing models, has been with Prof. C. Tong (Clemson University). Multi-scalar subgrid-scale (SGS) turbulent mixing, which must be modeled in LES, is being studied experimentally using a novel three-stream turbulent jet flowfield. Here, the main focus is on the SGS scalar filtered joint density function (essentially the subgrid-scale joint scalar distribution) and its statistics, including the passive-to-reactive SGS scalar time scale ratio, as they relate to LES of turbulent multi-scalar mixing and reacting flows. Planar Rayleigh scattering and acetone PLIF, from frequency-doubled (532 nm) and frequency-quadrupled (266 nm) Nd:YAG lasers, are used for to image the inner and outer co-annular jets issuing into a low-speed coflow. Both are imaged with a single interline-transfer CCD camera (PCO 1600) having excellent quantum efficiency (~55%) and read-noise characteristics (~11 e^-). The laser pulses are separated in time by 250 ns, enough time for charge to be transfered from light-sensitive to storage pixels. Due to the desire for high spatial resolution, a special lens was configured consisting of Rodenstock *close-up* lens and a 58-mm f/1.2 Noct-Nikkor lens having an aspheric first element. Here, spatial resolution was determined to be ~85 μm, a number equaling two binned pixels in the 800×512 pixel array and one that is slightly smaller than the laser sheet thicknesses. A sample image pair is shown in Figure 25.

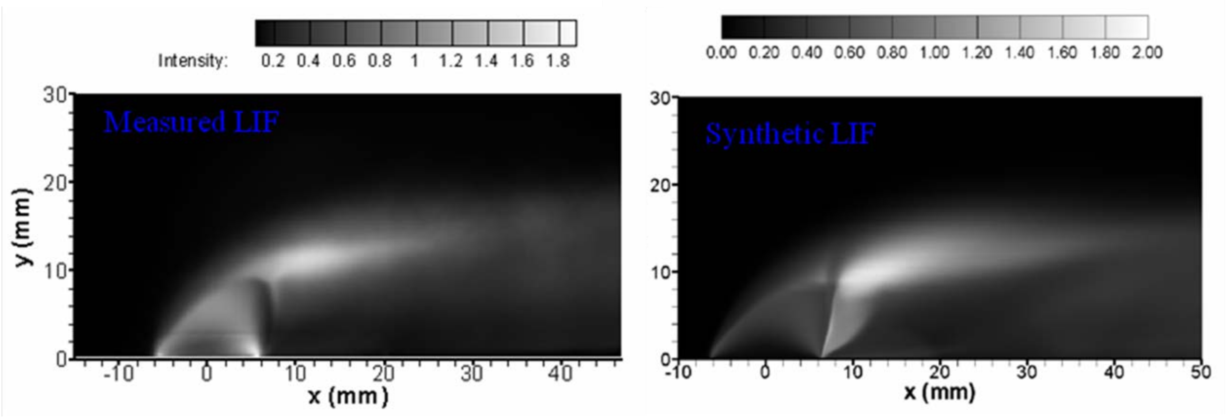

Figure 26: Comparison Between Measured and Computed LIF Signal.

The computed signal is based on computational conditions for T, P, V, injectant mole fraction, and the LIF equation relating signal strength (counts) to number density.

Even with this high spatial resolution, signal-to-noise ratios are high, 60-70 for "pure" jet fluid for images shown in Figure 25 (~600 mJ/pulse at 532 nm and 80 mJ/pulse at 266 nm). Jet-exit velocities are ~35 m/s, for these images, and the resulting displacement from one frame to the next is ≤ 9 μm (with $\Delta t = 250$ ns), a value much less than the image resolution. One can see that the core of the inner jet is intact at this downstream location (~17 to 39 mm above jet exit). Sample sets consist of up to 4000 images pairs. It should be noted, however, that high acetone concentrations lead to some undesirable effects, including 266-nm beam absorption, *enhanced* Rayleigh scattering from the *air* jet (inner jet in Figure 25), and acetone mass loading that is significant and potentially varying during the measurement time; as a consequence, limiting the acetone concentration well below saturation is necessary. This research—by providing a validation database—will make a significant contribution to the understanding of multi-scalar SGS mixing and will therefore improve the capability of LES to predict SGS mixing and turbulence-chemistry interactions. This work is described in more detail in Refs. 72 and 108.

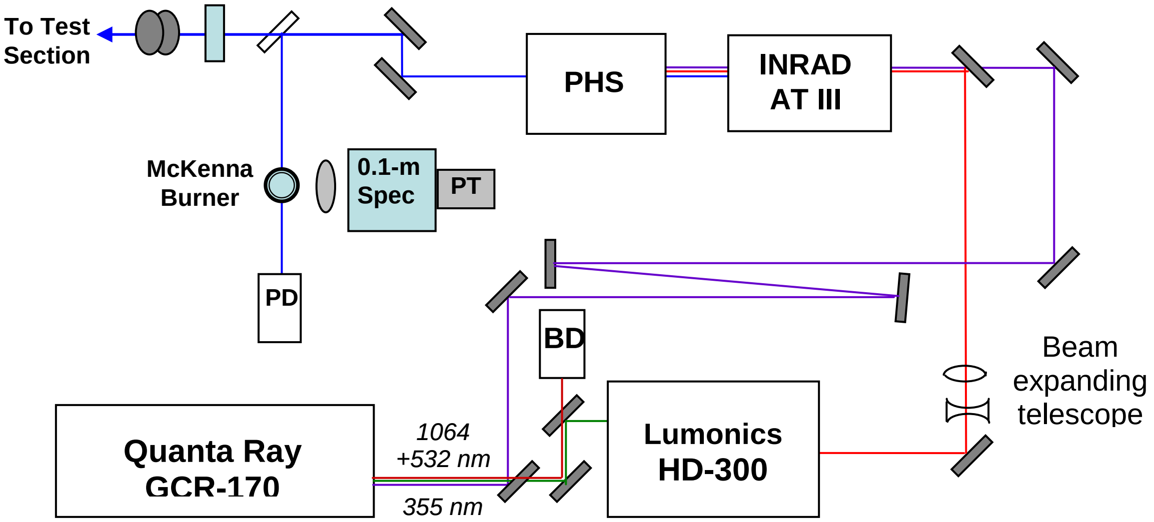

Figure 27: Optical Layout for Improved NO PLIF Diagnostic.

An example of recent efforts to use laser diagnostics to advance and validate modeling is shown in Figure 26. These images depict injection from a diamond-shaped injector into a Mach-2 crossflow [52, 69] and were described above (related to the description of Figures 1, 14, and 15). Here, PLIF of NO (the intensity scale is not calibrated) is compared to a synthetic PLIF image created from the original CFD simulation of flowfield temperature, pressure, velocity, and injectant mole fraction. One interesting aspect of this modeling is that it reveals the role that collisional line broadening plays in cases with a significant variation in pressure throughout the flowfield. As the pressure varies from sub-atmospheric values (in the freestream) to those of several atmospheres (near the injector exit), the NO $A^2\Sigma^+ \leftarrow X^2\Pi$ ($v'=0$, $v''=0$) ro-vibronic transition broadens beyond the laser linewidth, and the laser excitation rate decreases (and the fluorescence signal decreases accordingly). The result is that the laser coupling varies throughout the flowfield and the PLIF image cannot easily be related to injectant mole fraction. This effect can be seen in Figure 26: the signal varies within the bow-shock region where the injectant mole fraction is constant (i.e., $X_{\text{inj}} = 1$).

Thus, a model was developed to describe the LIF dependence on pressure, temperature, mixture composition, and velocity. The model relies upon literature values of electronic quenching cross sections and collisional broadening coefficients. While there is a reasonably good database for basic values, low-temperature (below 300 K) electronic quenching cross sections were heretofore lacking, and thus collaboration with Dr. T. Settersten, Sandia National Laboratories (Combustion Research Facility) was initiated. NO A-state (v=0) quenching rates were measured between 125 and 294 K in a custom, low-temperature cryostat [46] designed and fabricated for this study. Regarding the aforementioned figure, it is noted that the agreement between the two images is reasonably good. This comparison now clearly shows the differences between the computation and measurement that were not apparent with the original mole fraction computation (e.g., compare the bottom two images in Figure 1).

It is noted that in this most recent effort employing the NO PLIF technique, a new approach was implemented that dramatically simplifies the application of the technique. The new optical layout is shown in Figure 27. Previously, the dye laser operated at 574 nm (instead of 622 nm), and to generate output at 226 nm required that one first frequency double the dye laser output (to generate 287-nm radiation) and then mix this beam with the residual 1064-nm beam of the Nd:YAG laser. Typical output energies were 2 to 6 mJ/pulse at 226 nm. With the current scheme, the third harmonic of the Nd:YAG is employed (355 nm). This beam is frequency mixed within a BBO nonlinear crystal with the 622-nm dye laser beam; the dye laser is still pumped by the Nd:YAG second harmonic (532 nm). Not only is this approach easier to implement than the previous one, it is also more efficient, as > 10 mJ/pulse is easily generated.

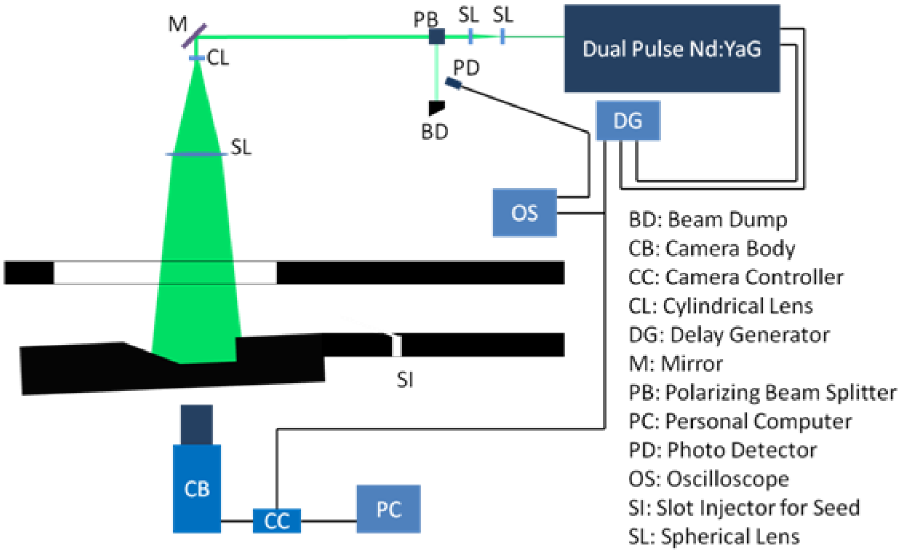

Figure 28: Schematic of PIV Layout for Probing Cavity Flameholder in Mach-2 Crossflow [98].

For some time a focus for this program has been on the quantification of the behavior of a cavity flameholder in a high-speed crossflow. Many measurements have been made to characterize the burning pattern, using OH PLIF, for a range of fueling conditions. Efforts have also been expended to quantify the flowfield, but this has proved difficult. Hydroxyl tagging velocimetry (HTV) has been used successfully under nonreacting conditions, but HTV cannot be used easily within the reacting cavity, due to competition with the super-equilibrium OH that is produced at the flamefront (as noted above). PIV has been used too, with some success, in the nonreacting flowfield, though uniform seeding of the entire duct is impractical. In the reacting cavity, application of PIV has proved to be more challenging: a principal difficulty is that the windows are readily fouled (within seconds). The problem may be exacerbated by softening of the windows (fused silica) under reacting conditions and a propensity of the particles to then stick to the windows (and potentially cause surface damage). Nonetheless, due to the importance of flowfield characterization, there is a renewed interest in implementing PIV in high-speed combustors.

A schematic of the setup is shown in Figure 28: the laser sheet was introduced into the Research Cell 19 tunnel through the top window, and scattering was imaged, using a PCO-1600 CCD camera, through a side-window that can be readily cleaned or replaced. Titanium-dioxide (TiO_2) was chosen a seed material, after comparison with other potential materials (e.g., Al_2O_3). The seed particles were spherical, which reduces their propensity to agglomerate and to stick to surfaces, and nominally 0.1 μm in diam., a size that provides a reasonable compromise between

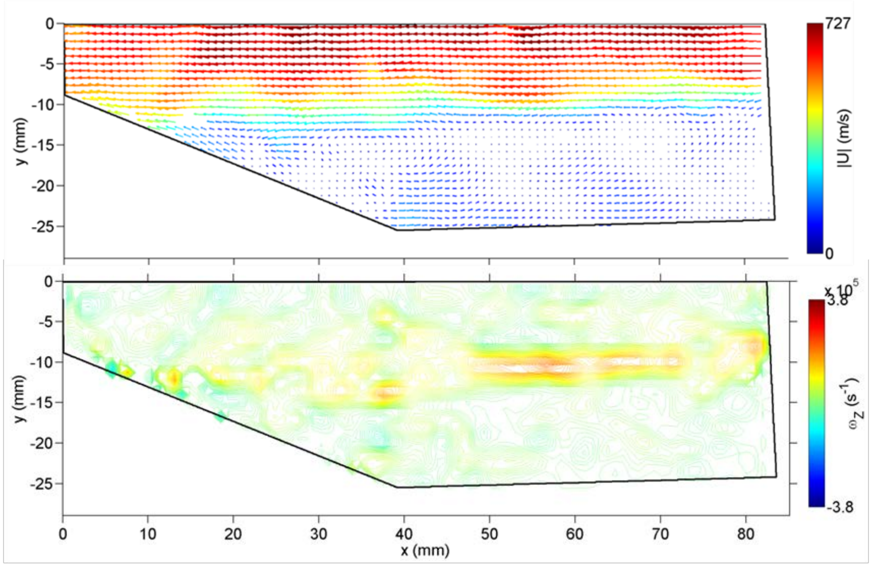

Figure 29: Sample Velocity (Top) and Vorticity (Bottom) Fields in a Reacting Cavity.

scattering cross section and flow-tracking. A particular challenge in PIV with an internal flow is in achieving particle seed density that is sufficient for good data-yield but not so high as to rapidly cloud windows; indeed, this problem is sufficiently challenging that there have been no other published works (to our knowledge) with a reacting cavity flowfield. A novel solution was found for introducing 0.1-μm-diameter spherical TiO_2 particles into the shear layer that forms over the cavity: use of a low-angle, 25-mm-wide slot positioned well upstream of the cavity. Entrainment of the seeded boundary/shear-layer fluid ensured good particle distribution within the cavity, especially within the central core, and the rate of window obscuration (from the particles) was modest, such that a few 30-second combustion runs (wherein 425 velocity measurements were recorded for each) could be executed before the windows required cleaning or replacement. The resulting seed level was sufficient to process the images (using LaVision DaVis 7.2 software) with interrogation regions of 32×32 pixels. Velocity fields were recorded for a range of fuel flow rates, and parameters such as vorticity, dilation, Reynolds stress, etc., were derived for each of the four cases studied (with various fueling levels). Instantaneous images revealed a highly unsteady, three-dimensional flowfield for all conditions, with significant out-of-plane motion. The average and variance of the velocity and vorticity revealed a number of behaviors that were altered by combustion and showed a dependence on the location and intensity of combustion. While not apparent in the instantaneous views, the average velocity path lines revealed the primary recirculation zone predicted in time-averaged numerical investigations. The interaction of the high momentum bulk flow and the volumetric expansion accompanying heat release along the shear layer and around the ramp, where the shear layer impinged, compressed the primary recirculation zone and produced a shallower impingement angle with increasing fuel flow (and heat release). Because there has been a dearth of cavity-flameholder velocity data reported in the literature, this data will be especially valuable for validation of CFD models.

Sample instantaneous vector and vorticity maps (duct centerline) are shown in Figure 29 for a condition with an C_2H_4 flow of 99 standard liters/minute into the cavity (from ramp-face ports), corresponding to a moderately high fueling rate (~3 times the value for lean blowout). The field of view includes nearly the entire cavity and a portion of the free stream, where $V_x \approx 730$ m/s for Mach-2 freestream conditions. The laser pulse separation was set to ~2 μs to allow sufficient displacement of the particles within the cavity, and numerous large scale features can be seen. A more complete description of the work is given in Ref. 98, which received an AIAA Best Paper Award for 2011.

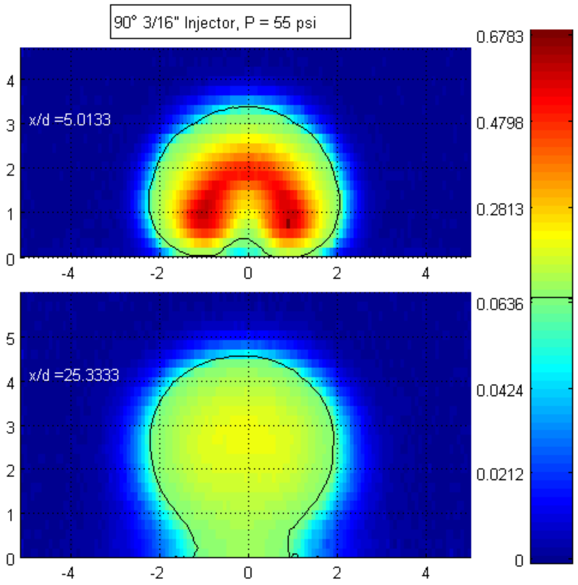

Figure 30: Distribution of Fuel (Mixture Fraction) from a Normal, 4.8-mm-Diam (d) Injector into a M-2 Crossflow at Two Downstream Locations.

Injection pressure is 3.7 atm. Axes are spanwise (z) and height (y) location divided by injector diam. The black line represents the stoichiometric contour.

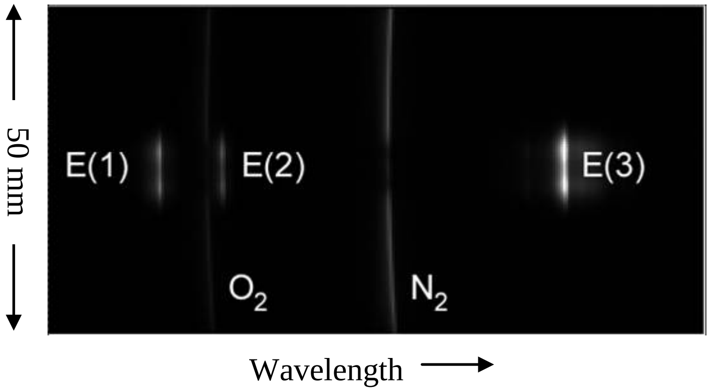

Figure 31: Raman Scattering Spectrum at x/d = 5.0.

Vertical axis is the spatial dimension (along the beam path); horizontal axis is the spectral dimension. The N_2 line is at 607 nm; the C-H stretch line for C_2H_4 [E(3)] is at 634 nm.

A similar effort was undertaken to provide our in-house CFD group and the larger modeling community with a quantitative dataset of injection (into a high-speed, Mach-2 crossflow). In this case circular injectors with two inclination angles (30 and 90 degrees) were designed for study. Line-Raman imaging—that is, imaging the scattering along the line defined by the laser beam—was chosen as the measurement tool since one can derive mole or mass fraction of injectant by measuring spontaneous Raman scattering for nitrogen (N_2) and the fuel (C_2H_4). To create the 2D image shown in Figure 30, individual 1D measurements, each requiring a 20-s exposure from a 5-W continuous-wave laser (Coherent Verdi), at different heights (in 0.5- to 1-mm increments) from the tunnel floor are assembled into a 2D image. Spontaneous vibrational Raman scattering is collected with Nikon lens and dispersed within a high-efficiency Kaiser HoloSpec f/1.8 spectrometer equipped with a holographic transmission grating. Vibrational Raman features are detected with a back-illuminated, electron-multiplying CCD camera (Andor iXon); the length of the laser-line image depends on the slit height and system magnification and here was set to about 51 mm. A sample spectrum is shown in Figure 31, and one can “see” the characteristic “kidney-shaped” structure of the injectant plume that is also apparent in Figure 30 (top image).

Calibration of Raman signals, a critical step for quantitative measurements, was accomplished in a two-step process: 1) measure air scattering (nitrogen) at room conditions; 2) add C_2H_4 to the tunnel (loosely “sealing” tunnel with foam), allow it to mix, and again measure Raman signals. C_2H_4 number density was then calculated from the decrease in nitrogen signal. These images form a database for CFD model validation, and accordingly the data set has been made available to all interested modelers. It should be noted that while line-Raman imaging, as employed here to derive 2D images of injectant concentration, is a powerful technique for obtaining quantitative mixing data, the NO PLIF technique allows one to obtain the entire mixing field (though in a less quantitative manner) in a 10-ns snapshot. Clearly the combination of the two techniques provides an excellent mixing database for CFD development/validation in general and LES development/validation in particular. More details of this work are given in Refs. 53 and 70; the journal article is based on AIAA paper that received a *Best Paper* Award.

Finally, the PM for this program, Dr. Campbell Carter, participated in the AFOSR Windows on Europe (later renamed Windows on the World) program in 2008 (7 weeks), 2009 (4 weeks), and 2011 (2 weeks). He worked with personnel at the Deutsches Zentrum fur Luft- and Raumfahrt (German Aerospace Center or DLR) at the Stuttgart facility; principally this included Drs. Wolfgang Meier and Isaac Boxx (a former NRC Postdoctoral Research Associate). The intent was to explore kHz-framing PLIF and PIV; the DLR-Stuttgart has become a world leader in the effort to develop and apply kHz-framing PLIF and PIV to combustion devices. The target flame for 2008 and 2009 efforts was that stabilized in a swirl burner; the burner used in 2008 is shown in Figure 32. Figure 33 shows the optical layout for the measurements. Here, the PIV system employs a dual-cavity, diode-pumped EdgeWave Nd:YAG laser (ISS-611DE), while the OH PLIF laser system employs a short-pulse (i.e., ~8 ns) EdgeWave Nd:YLF pump laser (IS-811E) and a Sirah Cobra-Stretch dye laser [48]. It is noted that this system was upgraded in 2009, with the addition of a new PLIF system (including a new pump laser based on a Nd:YAG system and a new dye laser, the Sirah Credo), operating at 10 kHz and with higher pulse energies (up to 200 μJ).

Timing separation for the PIV pulses was set to achieve a reasonable particle displacement (of a few pixels), and this equated to Δt_{PIV} = 20 or 30 μs; the PLIF laser pulse was located between the PIV pulses in time. While the dye laser’s optical path is equivalent to the version used at a 10-Hz pump frequency—and uses a single dye cell in a oscillator/pre-amplifier configuration—it did include a high-capacity pump to replace the dye in the pump region between consecutive pump laser pulses to ensure good dye laser efficiency. The dye laser output at 566 nm was frequency doubled by focusing the dye beam into a BBO crystal to obtain reasonable conversion efficiency. The dye laser was tuned to the strong $Q_1(7)$ ro-vibronic transition within the $A^2\Sigma^+–X^2\Pi$ ($v'=1,v''=0$) band. For these measurements at 5 kHz, the pulse energies were about 0.1 mJ at 283 nm and 2.6 mJ (each) at 532 nm. As noted above, 10 kHz systems are now available that also provide higher output energy at 283 nm (the exact value depending on the pump-beam pulse energy).

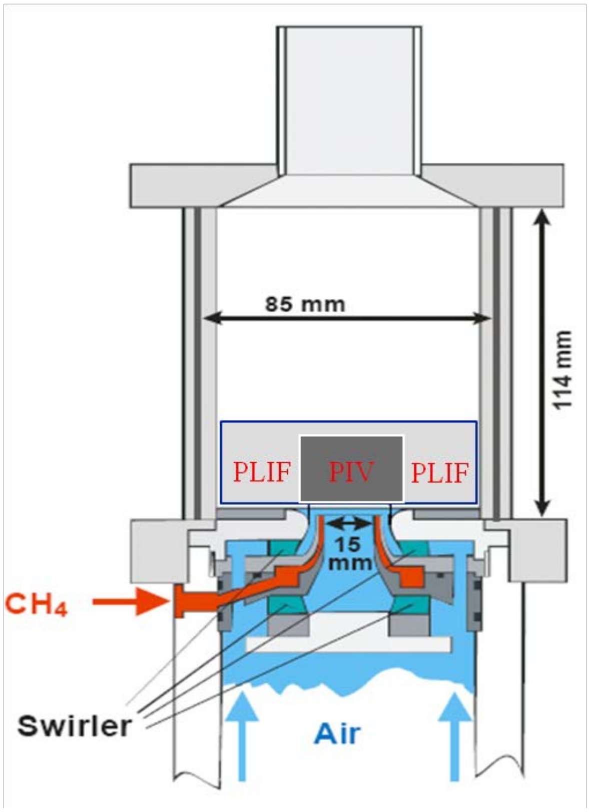

Figure 32: DLR Double-Swirl Burner.

OH fluorescence was recorded with a LaVision HSS6 digital camera, based on a CMOS (complimentary metal-oxide semiconductor) architecture, and an external, two-stage lens-coupled intensifier (LaVision HS-IRO). This camera array is composed of 1024×1024 pixels, each 20-µm square, and operates in full-frame mode at up to 5400 frames per second (fps). It is noted that CMOS-based cameras have significant advantages over CCD-based cameras in achieving high framing rates. The lens-coupled intensifier uses custom-designed coupling optics with an aperture sufficiently large to accommodate the 20.5-mm-square CMOS array. For these measurements the intensifier exposure was set to 500 ns; the gain was set to maximize the OH measurement dynamic range, though in some cases, saturation of the sensor was observed. A Cerco 45-mm f/1.8 UV lens was attached to the intensifier to capture the OH fluorescence; elastic scattering along with fluorescence from the OH A–X (1,0) band was blocked using a high-transmission (> 80% at 310 nm) bandpass interference filter (Custom fabrication - Laser-

Components GmbH) and a Schott glass filter (1-mm-thick WG295). The OH PLIF field of view was set to cover the width of the swirl flame chamber, about 86×86 mm^2.

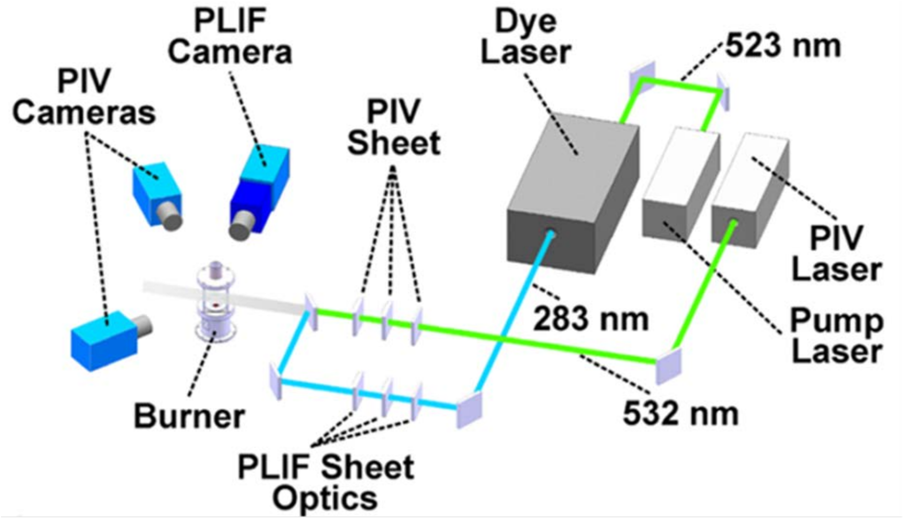

Figure 33: Optical Layout for 2008 DLR KHz Laser System [48].

Particle scattering (for PIV) was recorded with a pair of LaVision HSS5 CMOS cameras arranged in a forward-scattering, stereo configuration. TiO_2 particles were added to both the jet and coflow streams to ensure good seeding throughout the flowfield. The PIV cameras were equipped with Tokina 100-mm focal length lenses set to an f-stop of f/5.6, and in both cases the camera and lens were mounted on a Scheimpflug adaptor to mitigate image blur. No optical filtering was required for the PIV measurements, since the exposure was relative short at 0.1 ms. The HSS5 CMOS camera has a 1024×1024 pixel array that can be read out at 3 kfps; however, to acquire velocity images at 5 kHz, it was necessary to read out only a portion of the array at 10 kfps and thus reduce the frame size to 512×512 pixels. The field of view of the PIV cameras was set to cover a region of about 32 mm (wide) × 30 mm (high). Good seed density allowed the image pairs to be processed with 16-pixel interrogation regions, giving a reasonable spatial resolution of about 1 mm. One significant advantage to kHz PIV is that the dynamic range of velocity measurements can be extended to capture low velocities by correlating images from the next set of laser pulses (or potentially subsequent pulses), occurring, in this case, 200 µs later. The approach of using the subsequent laser pulse requires that the images be processed in two steps: 1) for high V and 2) for low V.

Shown in Figure 34 are six consecutive images from the DLR Double-Swirl burner, fueled with CH_4. Here, the velocity field is represented by red and green vectors (red and green intensity represent the out-of-plane velocity magnitude), while the flamefront, as derived from the edge-filtered OH PLIF image, is shown by the red-yellow “band”. These remarkable images reveal a dynamic flame; *proper orthogonal decomposition* of the velocity field reveals that within different regions of the flow, there are very strong velocity spectral peaks that correspond to a) the strong thermoacoustic (TA) pulsations (at 308 Hz) and b) precessing vortex (PV), at 515 Hz. Indeed different regions of the combustor show distinct spectra. Study of TA pulsations is motivated by the fact that these strong pressure oscillations can cause damage to the combustor (in the most extreme cases) and thus can limit the operation of the combustor (to nondestructive

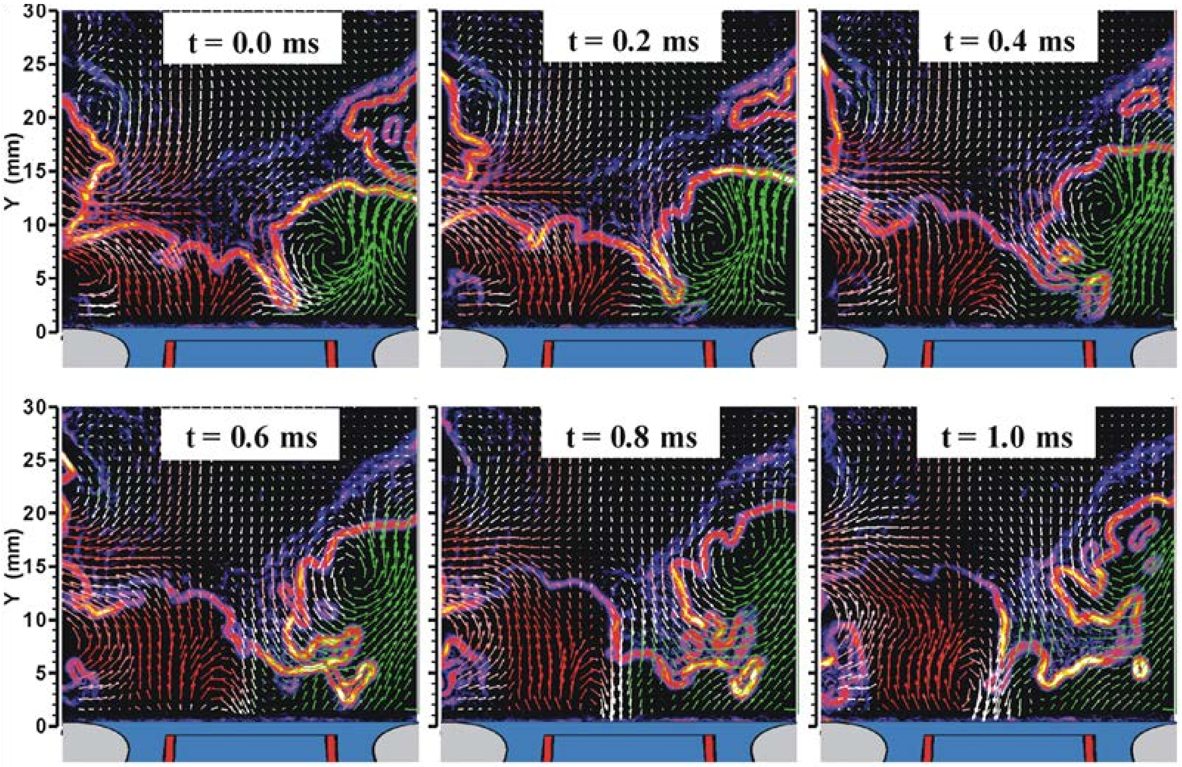

Figure 34: Sample set of PIV and OH PLIF Images in DLR Double-Swirl Burner [64].

conditions). One interesting conclusion from this work is that when one considers both TA and PV phases jointly, the flame topology is reasonably repeatable. More details can be found in Refs 68, 76, 86, 92, 93, 97, and 105.

When this combustor is operated at a global equivalence ratio of 0.55, the flame undergoes periodic extinction (lean blowout) and then re-attachment. For the first time, this process was studied in detail, and an improved understanding of extinction was thus derived. It was found that near lean blowout there are essentially two regions where reaction takes place, namely the helical zone along the PV and the *flame root* around the lower stagnation point. The zone along the PV is favorable to the flame due to low strain rates in the vortex center and accelerated mixing of burned and fresh gas. The flame root, which is located close to the nozzle exit, is characterized by an opposed flow of burned gas and relatively fuel-rich fresh gas. Due to the presence of high strain rates, the flame root is inherently unstable near lean blowout, featuring frequent extinction and reignition. The blowout process starts when the extinction of the flame root persists over a critical length of time. Subsequently, the reaction in the helical zone can no longer be sustained and the flame finally blows out. The results highlight the crucial role of the flame root and suggest that well-aimed modifications of flow field or mixture fraction in this region might shift the lean blowout limit to leaner conditions. This work is described in more detail in Ref. 76, which was chosen as the *Distinguished Paper* within the IC Engines Colloquium of the 33rd International Symposium on Combustion.

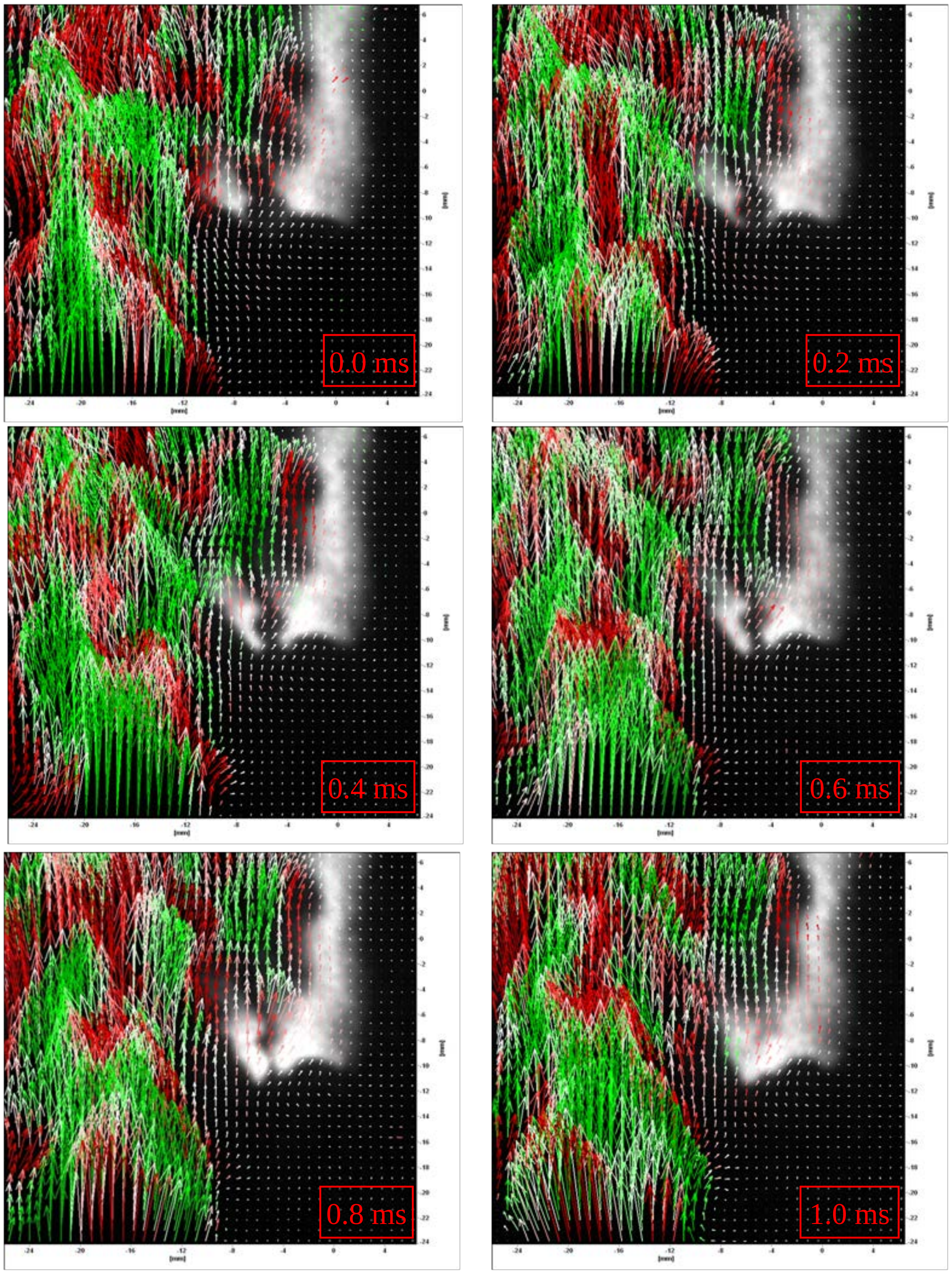

Figure 35: Simultaneous Measurement of OH (Shown in White) and the Velocity.

Some time was also devoted to the study of the canonical lifted jet flame in 2008, and 2010, and 2011. Stabilization of the lifted jet flame has been the subject of much research, and much controversy still exists over the exact mechanism. Our efforts included measurements over a range of jet exit Reynolds numbers (Re_j) with a laser setup as shown or similar to that in Figure 33. Shown in Figure 35 are 6 consecutive images from a lifted jet flame. While the OH PLIF system captured both sides of the flame (OH is shown as the white band against the black background), the PIV field of view was set to interrogate the right-hand side of the flame only. Propane, C_3H_8, (X=75%) diluted with argon, Ar, (X=25%) was the fuel; the jet exit velocity was about V_{jet} = 26.6 m/s and the corresponding Re_j was 15,000. The jet issued into a low-speed (V_{exit} = 0.2 m/s) air coflow. The high-speed region is shown with elongated vectors (red and green intensity are used to indicate the out-of-plane velocity component, V_z); the flame, on the other hand, stabilizes in a region of relatively low speed gas. It is seen here that at the flame base, that a hole that has formed in the OH layer *heals* over a span of < 1 ms. The processes of hole formation and *healing* are of great interest to both experimentalists and modelers.

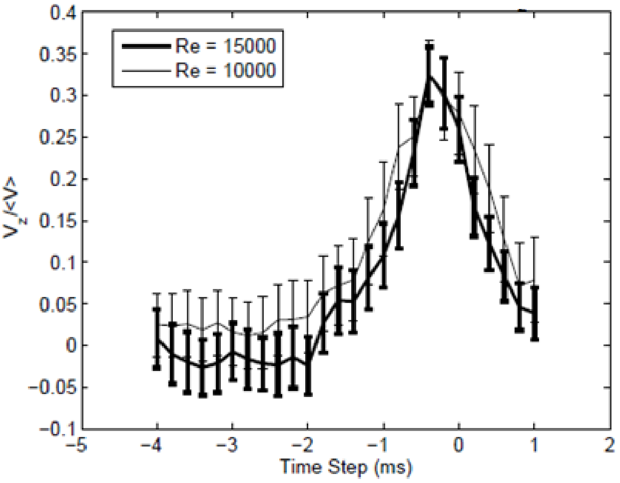

Figure 36: Time History of Flame-Jumps in a Lifted Jet Flame, Shown with the Out-of-Plane Velocity Component, V_z [96].

Measurements performed in 2008 showed that the flame is often moving downstream (about 2/3 of the time) and that significant upstream flamebase movement coincides with so-called flame-jumps, where the flame appears upstream of the previous stabilization point [96]. While some researchers have attributed this behavior to out-of-plane effects, other mechanisms such as autoignition cannot be ruled out. Fortunately, long-duration (~1-s record length) high-speed measurements such as these allow new ways of analyzing flame behavior. For example, one can focus on the flowfield preceding the occurrence of a flame-jump. Figure 36 shows the out-of-plane velocity component V_z just upstream of the flame stabilization point in the time surrounding a flame-jump. It is seen that V_z begins to increase ~2 ms before the jump, indicating the importance of out-of-plane effects in stabilization. The focus for 2010 was thus to better understand these effects. The optical layout was such that one camera viewed OH LIF in a normal manner; the second camera was oriented to view OH chemiluminescence on the laser entry and exit flame surfaces. The timing gate for the second camera was set to capture both chemiluminescence and LIF. The range of Re_j for the fuel jet (C_3H_8-Ar mix) was 15,000 – 30,000. Both fuel and coflow-air were seeded with 1-μm TiO_2 particles.

Two image pairs are shown in Figure 37 from a flame with a Re_j = 20,000; in both image pairs, the combined chemiluminescence + PLIF is shown on the left. In the left-hand pair, one sees both the distorted leading edge of the flame and a flame-hole that has crossed the laser probe plane (most holes do not cross the plane, of course). From images such as these (in particular the movies created from individual images), it is now clear that distortions of the flamebase lead to the observation of flame-jumps. Indeed, one such jump is shown in the right-hand image pair, and it now seems clear that flame-jumps occur due to the wrinkling/distortion of the flamebase and that out-of-plane effects are dominant at the flame base. The OH that appears at (jumps to) a new upstream location moves into the field of view of the planar measurement from out of the laser plane. This observation resolves an especially troubling observation from 2008: the flame was observed to moved downstream often but did not seem to propagate upstream. Clearly, experimentalist will have to better address 3D effects in turbulent flames to fully understand their propagation, stabilization, extinction, etc.

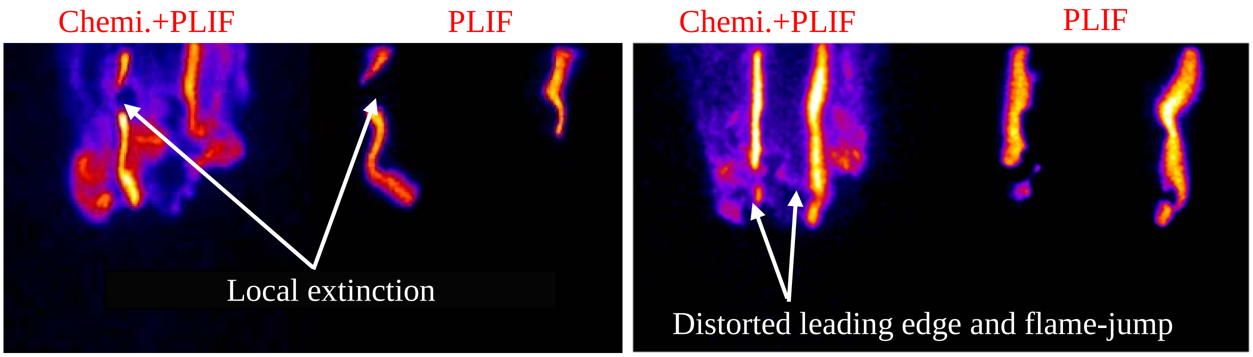

Figure 37: Two Pair of Instantaneous Combined Chemiluminescence (Left) + PLIF (Right) Images from a Flame with Re_j=20,000.

The left-hand pair shows an example of local extinction; the right-hand pair shows an example of a flame-jump in progress.

5 CONCLUSIONS

This basic research task on supersonic combustion ramjets includes work in three primary focus areas: *i*) ***Fuel Control and Fuel Injection***, wherein fundamental aspects are studied for gaseous, supercritical, and multiphase fuels; *ii*) ***Ignition, Flameholding, and Flame Propagation in Supersonic Flows***, wherein fundamental aspects are studied with a view towards improving performance in a high-speed combustor; and *iii*) ***Multidisciplinary Laser Measurements*** for benchmarking modeling and simulation and for elucidating the physics of high-speed flows. The motivation for this program was the need to develop the science basis to enable the design of high-speed, air-breathing propulsion systems. Much progress has been made in improving the science basis for high-speed propulsion. Our fundamental understanding has been improved for fuel injection (for liquid, gas, and two-phase flows); plasma-enhanced combustion, and flameholding in high-speed flows. Additionally, we applied advanced diagnostics—including X-ray techniques (phase contrast imaging, radiography, and small-angle X-ray scattering), planar laser-induced fluorescence (PLIF), particle image velocimetry (PIV), spontaneous Raman scattering, etc.—in novel ways to probe turbulent flows (relevant to high-speed propulsion). Furthermore, this program, through our interaction with the German Aerospace Center (DLR-Stuttgart), has significantly advanced diagnostics in the area of high-frequency planar measurements. Not only has this work demonstrated the efficacy of the approach, it has employed kHz OH PLIF an PIV to study complex turbulent reacting flowfields, including swirl stabilized flames and the turbulent lifted jet flame. The reader is encouraged to look at the large body of work that has derived from this program, to better appreciate the full depth of the research conducted during the course of the program.

6 RECOMMENDATIONS

In spite of the progress made during this program, several outstanding research areas should be addressed in an upcoming program. These include the following items.

1. Our understanding of aerated sprays has increased substantially through the use of advanced diagnostics that include digital holography, phase-contrast imaging, X-ray radiography, and ballistic imaging. However, most of our efforts have involved aerated jets in a quiescent flow. Future efforts are now being planned to use radiography at the APS to probe a jet in crossflow.

2. Likewise, our understanding of supercritical sprays has increased substantially with the use of small-angle X-ray scattering (SAXS). We now better understand the nucleation process vis-à-vis the formation of droplets and their sizes. Nonetheless, our SAXS measurements have been limited in their dynamic range by the SAXS instrumental configurations at the Advanced Photon Source (APS). Upgrades to the 12-ID beamline at the APS should substantially improve the dynamic range for droplet size measurements, and we await future opportunities to use this upgraded instrument.

3. We have demonstrated the utility of spontaneous Raman scattering for quantitative measurements of fuel injection into a high-speed flow. The modeling community has made great use of the measurements, and there is a continuing pull to provide more quantitative data. Therefore, it will be important for continued model development to continue to provide quantitative data that should include concentrations and velocity fields.

4. Understanding dynamic processes such as blowout and ignition has been aided in the last several years by the advent of high-framing-rate diagnostics. Future resources should be expended to extend the interrogation frequencies beyond 10 kHz, for planar laser-induced fluorescence (PLIF) and particle image velocimetry (PIV), so that a wider range of combustion problems can be addressed. Indeed, blowout and ignition could be studied in detail to provide a detailed understanding of these processes (for example in scramjet cavity flameholder), much as has been done in the DLR swirl burner experiments.

7 REFERENCES

1. Rasmussen, C. C., Driscoll, J. F., Hsu, K.-Y., Donbar, J. M., Gruber, M. R., Carter, C. D., **“**Stability limits of cavity-stabilized flames in supersonic flow,” *Proceedings of the Combustion Institute.* **30**, 2825 (2005).
2. Rasmussen, C.C., Driscoll, J.F., Carter, C.D., and Hsu, K.-Y., “Technical Note: Characteristics of a cavity-stabilized pilot flame in a supersonic flow,” *Journal of Propulsion and Power* **21**, 765 (2005).
3. Murugappan, S., Gutmark, E., and Carter, C.., “Control of penetration and mixing of an excited supersonic jet into a supersonic cross-stream,” AIAA Paper 2005-0612, Jan. 2005.
4. Pitz, R. W., Lahr, M. D., Douglas, Z. W., Wehrmeyer, J. A., Hu, S., Carter, C. D., Hsu, K.-Y., Lum, C., and Koochesfahani, M., “Hydroxyl tagging velocimetry in a Mach 2 flow with a wall cavity, AIAA Paper 2005-36, Jan. 2005,
5. Tam, C.-J., Cox-Stouffer, S., Lin, K.-C., Gruber, M., and Jackson, T. A., “Gaseous and liquid injection into supersonic crossflows,” AIAA Paper 2005-0301, Jan. 2005.
6. Liu, J.T.C., Rieker, G.B., Jeffries, J.B., Hanson, R.K., Gruber, M.R., Carter, C.D., and Mathur, T., “Near-infrared diode laser absorption diagnostic for temperature and water vapor in a scramjet combustor,” *Applied Optics* **44**, 6701 (2005).
7. Rieker, G. B., Liu, J. T. C., Jeffries, J. B., Hanson, R. K., Mathur, T., Gruber, M. R., and Carter, C. D., “Wavelength-multiplexed tunable diode laser sensor for gas temperature and H_2O concentration in a scramjet combustor,” AIAA Paper 2005-3710, July 2005.
8. Montes, D. R., King, P. I., Gruber, M. R., Carter, C. D., and Hsu, K.-Y., “Mixing effects of a pylon placed upstream of a flameholding cavity in a supersonic flow,” AIAA Paper 2005-3913, July 2005.
9. Allen, W. H., King, P. I., Gruber, M. R., Carter, C. D., and Hsu, K.-Y., “Fuel-air injection effects on combustion in cavity-based flameholders in a supersonic flow,” AIAA Paper 2005-4105, July 2005.
10. Star, A.M., Edwards, J.R, Lin, K.-C., Cox-Stouffer, S., and Jackson, T.A. “Numerical simulation of injection of supercritical ethylene into nitrogen,” *Journal of Propulsion and Power* **22**, 809 (2006)
11. Lin, K.-C., Cox-Stouffer, S. K., Jackson, T. A., “Structures of phase transition processes of supercritical methane/ethylene mixtures injected into a subcritical environment,” *Combustion Science and Technology* **179**, 129 (2006).
12. Kahadawala, M.S.P., Corera, S.A.P., Williams, S., Carter, C.D., and Sidhu, S.S., “Investigation of kinetics of iso-octane ignition under scramjet conditions,” *International Journal of Chemical Kinetics* **38**, 194 (2006).
13. Ombrello, T., Qin, X., Ju, Y., Gutsol, A., Fridman A., and Carter, C., “Combustion enhancement via stabilized piecewise non-equilibrium gliding arc plasma discharge,” *AIAA Journal* **44**, 142 (2006).
14. Murugappan, S., Gutmark, E., Carter, C., Donbar, J., Gruber, M., and Hsu, K.-Y., “Transverse supersonic controlled swirling jets in a supersonic cross stream,” *AIAA Journal* **44**, 290 (2006).
15. Murugappan, S., Gutmark, E., and Carter, C., “Control and penetration and mixing of an excited supersonic jet into a supersonic cross-stream,” *Physics of Fluids* **17,** 106101 (2005).
16. Pitz, R.W., Lahr, M.D., Douglas, Z.W., Wehmeyer, J.A., Hu, S., Carter, C.D., Hsu, K.-Y., Lum, C., and Koochesfahani, M.M., “Hydroxyl tagging velocimetry in a Mach 2 flow with a wall cavity,” *Applied Optics* **44**, 6692 (2005).
17. Lahr, M.D., Pitz, R.W., Douglas, Z.W, and Carter, C.D., “Hydroxyl tagging velocimetry in a Cavity-piloted Mach 2 combustor,” AIAA Paper 2006-0040, Jan. 2006.
18. Wu, P.-W., Lin, K.-C., and Jackson, T.A., “Effects of flow initial conditions on spray characteristics with and without crossflows (Invited),” AIAA Paper 2006-1506, Jan. 2006.

19. Star, A. M., Edwards, J. R., Lin, K.-C., Jackson, T. A., “Modeling of condensation in injection of supercritical fuels,” AIAA Paper 2006-0810, Jan. 2006.
20. Haubelt, L.C., King, P.I., Gruber, M.R., Carter, C.D., and Hsu, K.-Y., “Performance of pylons upstream of a cavity-based flameholder in non-reacting supersonic flow,” AIAA Paper 2006-4679, July 2006.
21. Meicenheimer, H.L. Gutmark, E.J., Carter, C.D., Eklund, D.R., and Gruber, M.R., “A computational assessment of independent stage control of a cascade injector,” AIAA Paper 2006-4863, July 2006.
22. Sallam, K.A., Aalburg, C., Faeth G.M., Lin, K.-C., Carter, C.D., and Jackson, T.A., “Primary breakup of round aerated-liquid jets in supersonic crossflows,” *Atomization and Sprays* **16**, 657 (2006).
23. Jacobsen, L.S., Carter, C.D., and Dwenger, A.C., “Cavity-based injection mixing experiments for supersonic combustors with implications on igniter placement,” AIAA Paper 2006-5268, July 2006.
24. Leonov, S., Yarantsev, D., Starodubtsev, M., and Carter, C., “Mechanisms of fuel ignition by electrical discharge in high-speed flow,” AIAA Paper 2006-7907, Nov. 2006.
25. Steinberg, A.M., Driscoll, J.F., Micka, D.J., Ceccio, and Carter, C.D., “A cinema stereoscopic PIV system for the measurement of micro- and meso-scale turbulent premixed flame dynamics,” Paper B13, 5th US Combustion Meeting, The Combustion Institute, March 2007, San Diego, CA.
26. Miller, B., Sallam, K.A., Bingabr, M., Lin, K.-C., and Carter, C., “Secondary breakup of aerated liquid jets in subsonic crossflow,” AIAA Paper 2007-1342, Jan. 2007.
27. Busby, K, Corrigan, J., Yu, S.-T, Williams, S., Carter, C., Schauer, F., and Hoke, J., “Effects of corona, spark and surface discharges on ignition delay and deflagration-to-detonation times in pulse detonation engines,” AIAA Paper 2007-1028, Jan. 2007.
28. Anderson, T.N., Lucht, R.P., Meyer, T.R., Mathur, T., Grinstead, K.D., Gord, J.R., Gruber, M., and Carter, C.D., “Measurements of NO and OH concentrations in vitiated air using diode-laser-based ultraviolet absorption sensors,” AIAA Paper 2007-467, Jan. 2007.
29. Rieker, G.B., Jeffries, J.B., Hanson, R.K., Mathur, T., Carter, C.D., and Gruber, M.R., “Comparison of wavelength modulation and direct absorption spectroscopy for measurements of gas temperature in a scramjet combustor,” Paper G01, 5th US Combustion Meeting, The Combustion Institute, San Diego, CA, March 2007.
30. Lin, K.-C., Tam, C.-J., Boxx, I., Carter, C., Jackson, K., Lindsey, M., “Flame characteristics and fuel entrainment Inside a cavity flame holder in a scramjet combustor,” AIAA Paper2007-5381, July 2007.
31. Hsu, K.-Y., Carter, C.D., Gruber, M.R., and Barhorst, T., “Experimental study of cavity-strut combustion in supersonic flow,” AIAA Paper 2007-5394, July 2007.
32. Kobayashi, K., Bowersox, R.D.W., Srinivasan, R., Carter, C.D., and Hsu, K.-Y., “Flow field studies of diamond shaped fuel injector in a supersonic flow,” AIAA Paper 2007-5416, July 2007.
33. Kobayashi, K., Bowersox, R.D.W., Srinivasan, R., Carter, C.D., and Hsu, K.-Y., “Flowfield studies of diamond-shaped fuel injector in a supersonic flow,” *Journal of Propulsion and Power* **23**, 1168 (2007).
34. Cathey, C., Cain, J., Wang, H., Gundersen. M.A., Carter, C., and Ryan, M., “OH Production by Transient Plasma and Mechanism of Flame Ignition and Propagation in Quiescent Methane-Air Mixtures,” *Combustion and Flame*, **154**, 715 (2008)
35. Jacobsen, L.S., Carter, C.D., Baurle, R.A., Jackson, T.A., Williams, S., Bivolaru, D., Kuo, S., and Barnett, J., “Towards plasma-assisted ignition in scramjets,” *Journal of Propulsion and Power* **24**, 641 (2008).

36. Gruber, M.R., Carter, C.D., Montes, D. R., Haubelt, L.C., King, P.I., Hsu, K.-Y., "Experimental studies of pylon-aided fuel injection into a supersonic crossflow," *Journal of Propulsion and Power* **24**, 460 (2008).
37. Miller, B., Sallam, K.A., Bingabr, M., Lin, K.-C., and Carter, C., "Secondary breakup of aerated liquid jets in subsonic crossflow," *Journal of Propulsion and Power* **24**, 253 (2008).
38. Doster, J.C., King, P.I, Gruber, M.R., Carter, C. D., Hsu, K.-Y., and Ryan, M., "Experimental investigation of air and methane injection from in-stream fueling pylons," AIAA Paper 2008-4501, July 2008
39. Gruber, M.R., Carter, C. D., Ryan, M., Rieker, G. B., Jeffries, J., Hanson, R. K., Liu, J., Mathur, T., "Laser-based measurements of OH, temperature, and water vapor concentration in a hydrocarbon-fueled scramjet," AIAA Paper 2008-5070, July 2008.
40. Lee, J., Sallam, K. A., Lin, K.-C., and Carter, C. D., "Spray structure in near-injector region of aerated jet in subsonic crossflow," *Journal of Propulsion and Power* **25**, 258 (2009).
41. Ryan, M., Gruber, M., Carter, C., and Mathur, T., "Planar laser-induced fluorescence imaging of OH in a supersonic combustor fueled with ethylene and methane," *Proceedings of the Combustion Institute* **32**, 2429 (2009).
42. Rieker, G. B., Jeffries, J. B., Hanson, R. K., Mathur, T., Gruber, M. R., and Carter, C. D., "Diode laser-based detection of combustor instabilities with application to a scramjet engine," *Proceedings of the Combustion Institute* **32**, 831 (2009).
43. Gruber, M.R., Carter, C.D., Montes, D.R., Haubelt, L.C., and King, P.I., "Experimental studies of pylon-aided fuel injection into a supersonic crossflow," *Journal of Propulsion and Power* **24**, 460 (2008).
44. Sedarsky, D., Gord, J., Carter, C., Meyer, T., and Linne, M., "Fast-framing ballistic imaging of velocity in an aerated spray," *Optics Letters* **34**, 2748 (2009).
45. Doster, J. , King, P. I., Gruber, M. R., Carter, C. D., Ryan, M. D., and Hsu, K.-Y., "Experimental investigation of air and methane injection from in-stream fueling pylons," *Journal of Propulsion and Power* **25**, 885 (2009).
46. Settersten, T. B., Patterson, B. D., and Carter, C. D., "Collisional quenching of NO $A^2\Sigma^+(v'=0)$ between 125 and 294 K." *Journal of Chemical Physics* **130**, 204302 (2009).
47. Stockman, E. S., Zaidi, S. H., Miles, R. B., Carter, C. D., and Ryan, M. D., "Measurements of combustion properties in a microwave enhanced flame," *Combustion and Flame* **156**, 1453 (2009)
48. Boxx, I., Stöhr, M., Meier, W., and Carter, C., "Brief Communication: kHz flamefront and velocity-field measurements for the study of flames," *Applied Physics B* **95**, 23 (2009).
49. Lee, J., Sallam, K. A., Lin, K.-C., and Carter, C. D., "Spray structure in near-injector region of aerated jet in subsonic crossflow," *Journal of Propulsion and Power* **25**, 258 (2009).
50. Leonov, S., Yarantsev, D., and Carter, C., "Experiments on electrically-controlled flameholding on a plane wall in a supersonic airflow," *Journal of Propulsion and Power* **25**, 289 (2009).
51. Ryan, M., Gruber, M., Carter, C., and Mathur, T., "Planar laser-induced fluorescence imaging of OH in a supersonic combustor fueled with ethylene and methane," *Proceedings of the Combustion Institute* **32**, 2429 (2009).
52. Kobayashi, K., Bowersox, R.D.W., Srinivasan, R., Tichenor, N., and Carter, C., Experimental and numerical studies of diamond-shaped injector in a supersonic flow," AIAA Paper 2009-1420, Jan. 2009.
53. Lin, K.-C., Ryan, M., Carter, C., Gruber, M., Raffoul, C., "Scalability of ethylene gaseous jets for fueling high-speed air-breathing combustors," AIAA Paper 2009-1423, Jan. 2009. **Best Paper**, awarded by the *Air Breathing Propulsion Technical Committee.*

54. Lin, K.-C., Carter, C., Fezzaa, K., Wang, J., Liu, Z., “X-ray study of pure- and aerated-liquid jets in a quiescent environment,” AIAA Paper 2009-0994, Jan. 2009.
55. Boxx, I., Stöhr, M., Blumenthal, R., Carter, C., and Meier, W., “Investigation of a gas turbine model combustor by means of high-speed laser imaging,” AIAA Paper 2009-644, Jan. 2009.
56. Olinger, D., Sallam, K., Lin, K.-C., and Carter, C., “Effects of GLR on the spray in the near-injector region of aerated liquid jets in crossflow,” AIAA Paper 2009-1373, Jan. 2009.
57. Lin, K.C., Ryan, M., Carter, C., Sandy, A., Narayanan, S., Ilavsky, J., and Wang, J., “Small angle X-ray scattering (SAXS) on droplet size and liquid contents of condensed supercritical ethylene jets,” 11th ICLASS International Conference on Liquid Atomization and Spray Systems, Vail, CO, July 2009.
58. Lin, K.-C., Carter, C., Fezzaa, K., Liu, Z., and Wang, J., “Studies of pure- and aerated-liquid jets using the X-ray phase contrast imaging,” 11th ICLASS International Conference on Liquid Atomization and Spray Systems, Vail, CO, July 2009.
59. Sallam, K.A., Lin, K.-C., and Carter, C.D., “Spray diagnostics using double pulsed double-view digital holography, 11th ICLASS International Conference on Liquid Atomization and Spray Systems, Vail, CO, July 2009.”
60. Hsu, K.-Y., Carter, C.D., Gruber, M.R., and Tam, C.-J., “Mixing study of strut injectors in supersonic flows,” AIAA Paper 2009-5226, Aug. 2009.
61. Crafton, J., Fonov, S., Hsu, K.-Y., Carter, C., and Gruber, M., “Optical measurements of pressure and shear on a strut in supersonic flow,” AIAA 2009-5033, Aug. 2009.
62. Steinberg, A., Boxx, I., Stöhr, M., Meier, W., and Carter, C.D., “Analysis of flow-flame interactions in a gas turbine model combustor under thermo-acoustically stable and unstable conditions,” AIAA Paper 2010-7152, July 2010. **Best Paper**, awarded by the *Propellants and Combustion Technical Committee.*
63. Steinberg, A., Boxx, I., Stöhr, M., Carter, C. D., and Meier, W., “Flow-flame interactions causing acoustically coupled heat release fluctuations in a thermo-acoustically unstable gas turbine model combustor.” *Combustion and Flame* **157**, 2250 (2010).
64. Meier, W., Boxx, I., Stöhr, M., and Carter, C. D., “Laser-based investigations in gas turbine combustors,” *Experiments in Fluids* **49,** 865 (2010).
65. Linne, M., Sedarsky, D., Meyer, T., Gord, J., and Carter, C., “Ballistic imaging in the near-field of an effervescent spray,” *Experiments in Fluids* **49,** 911 (2010).
66. Hsu, K.-Y., Carter, C. D., Gruber, M. R., and Barhorst, T., “Experimental study of cavity-strut combustion in supersonic flow,” *Journal of Propulsion and Power* **26,** 1237 (2010).
67. Lahr, M.D., Pitz, R. W., Douglas, Z.W., Carter, C.D., “Hydroxyl tagging velocimetry measurements of a supersonic flow over a cavity,” *Journal of Propulsion and Power* **26**, 790 (2010).
68. Boxx, I., Stöhr, M., Meier, W., and Carter, C., “Observations on the time-dependent behaviour of a partially premixed swirl flame in a gas turbine model combustor,” *Combustion and Flame* **157**, 1510 (2010).
69. Kobayashi, K., Bowersox, R. D. W., Srinivasan, R., Carter, C. D., and Ryan, M. D., “Technical Note: Experimental and numerical studies of diamond-shaped injector in a supersonic flow,” *Journal of Propulsion and Power* **26**, 373 (2010).
70. Lin, K.-C., Ryan, M., Carter, C., Gruber, M., and Raffoul, C., “Raman scattering measurements of gaseous ethylene jets in Mach 2 supersonic crossflow,” *Journal of Propulsion and Power* **26**, 503 (2010).
71. Lin, K.C., Rajnicek, C., McCall, J., Carter, C., Fezzaa, K., “Exploration of Near-Field Structures of Aerated liquid jets in a quiescent environment using the x-ray technique, “presented at the ILASS

Americas 22nd Annual Conference on Liquid Atomization and Spray Systems, Cincinnati, OH, May 2010.

72. Dinger, M.J., Cai, J., Carter, C. D., Ryan, M. J., and Tong, C., "Experimental study of three-scalar mixing in a turbulent coaxial jet," *Journal of Fluid Mechanics* **685**, 495 (2011).
73. Sun, W., Uddi, M., Won, S. H., Ombrello, T., Carter, C., and Ju, Y., "Kinetic effects of nanosecond pulsed discharge assisted low temperature methane oxidation on the extinction limits of methane diffusion flames," Accepted, *Combustion and Flame.*
74. Hammack, S., Rao, X., Lee, T. and Carter, C., "Direct-coupled plasma-assisted combustion using a microwave waveguide torch," *IEEE Trans. Plasma Sci.* **39**, 3300 (2011).
75. Rao, X., Hammack, S., Carter, C., Grothohn, T., Asmussen, Jr., J., and Lee, T., Microwave-plasma-coupled re-ignition of methane-and-oxygen mixture under auto-ignition temperature," *IEEE Trans. Plasma Sci.* **39**, 3307 (2011)
76. Stöhr, M., Boxx, I., Carter, C., and Meier, W., "Dynamics of lean blowout of a swirl-stabilized flame in a gas turbine model combustor," *Proceedings of the Combustion Institute* **33**, 2953 (2011). **Distiguished Paper** within the IC Engines Colloquium of the Combustion Symposium.
77. Rao, X., Hemawan, K., Wichman, I., Carter, C., Grotjohn, T., Asmussen, J., and Lee, T., "Combustion dynamics for energetically enhanced flames using direct microwave energy coupling," *Proceedings of the Combustion Institute* **33**, 3233 (2011).
78. Sun, W., Uddi, M., Ombrello, T., Won, S.H., Carter, C., and Ju, Y., "Effects of non-equilibrium plasma discharge on counterflow diffusion flame extinction," *Proceedings of the Combustion Institute* **33**, 3211 (2011).
79. Lin, K.-C., Rajnicek, C., McCall, J., Carter, C., and Fezzaa, K., "Investigation of pure- and aerated-liquid jets using ultra-fast X-ray phase contrast imaging," *Nuclear Instruments and Methods in Physics Research A* **649,** 194 (2011).
80. Lin, K.-C., Ryan, M., Carter, C., Sandy, A., Naravanan, S., Ilavsky, I., and Wang, J., "Investigation of condensed supercritical ethylene jets using Small Angle X-ray Scattering (SAXS) technique," *Nuclear Instruments and Methods in Physics Research A* **649,** 219 (2011).
81. Boxx, I., Arndt, C., Carter, C.D., and Meier, W., "Highspeed laser diagnostics for the study of flamedynamics in a lean premixed gas turbine model combustor," *Experiments in Fluids,* available online.
82. Lin, K.-C., Rajnicek, C., McCall, J., Fischer, B., Carter, C., and Fezzaa, K., "Structures of aerated-liquid jets injected from various nozzle contours," AIAA Paper 2011-232, Jan. 2011.
83. Ombrello, T. M., Carter, C. D., and Katta, V., "Flame speed enhancement by $O_2(a^1\Delta_g)$," AIAA Paper 2011-240, Jan. 2011.
84. Sun, W., Uddi, M., Won, S. H., Ju, Y., Ombrello, T., and Carter, C., "Kinetic effects of non-equilibrium plasma on partially premixed flame extinction," AIAA Paper 2011-971, Jan. 2011.
85. Hammack, S., Rao, X., Williamson, Z., Lee, T., and Carter, C., "Laser diagnostics of plasma enhanced flames in a waveguide microwave discharge system," AIAA Paper 2011-1019, Jan. 2011.
86. Steinberg, A.M., Boxx, I., Stöhr, M., Carter, C.D., and Meier, W., "Thermo-acoustic phase-relationships in oscillating swirl flames from high-speed laser diagnostics," 7th US National Technical Meeting of the Combustion Institute, Atlanta, GA, March 2011.
87. Ombrello, T., Carter, C., and Katta, V., "Sub-atmospheric pressure burner platform for basic flame studies," Poster presentation, 7th US National Technical Meeting of the Combustion Institute, Atlanta, GA, March 2011.
88. Lin, K.-C., and Carter, C., "Structures and applications of aerated-liquid jets in air-breathing propulsion systems," ILASS Americas 23th Annual Conference on Liquid Atomization and Spray Systems, Ventura, CA, May 2011.

89. Ombrello, T., Carter, C., McCall, J., Schauer, F., Tam, C.-J., Naples, A., Hoke, J., and Hsu, K.-Y., "Pulsed detonation combustor in a supersonic cross-flow for enhanced mixing and ignition," AIAA Paper 2011-3713, June 2011.
90. Lin, K.-C., Ryan, M., Carter, C., Sandy, A., Narayanan, S., Ilavsky, J., and Edwards, J., "Effects of back pressure on condensed-phase properties within supercritical ethylene jets," AIAA Paper 2011-3906, June 2011.
91. Crafton, J., Forlines, A., Palluconi, S., Hsu, K.-Y., Carter, C., and Gruber, M., "Investigation of transverse jet injections in a supersonic crossflow using fast responding pressure-sensitive paint," AIAA Paper 2011-3522, June 2011.
92. Steinberg, A.M., Boxx, I., Stöhr, M., Arndt, C.M., Meier, W., Carter, C.D., "Influence of flow-structure dynamics on thermo-acoustic instabilities in oscillating swirl flames," AIAA Paper 2011-5554, July 2011.
93. Stöhr, M., Boxx, I., Carter, C., and Meier, W., "Dynamics of vortex-flame interaction in a turbulent swirl flame," 5th European Combustion Meeting, Cardiff University, July 2011.
94. Boxx, I., Arndt, C., Carter, C., and Meier, W., "Out-of-plane flame sheet visualization in highspeed PIV/PLIF measurements of a lifted turbulent jet flame," Poster presentation, Gordon Research Conference on Laser Diagnostics in Combustion, Waterville Valley, NH, Aug. 2011.
95. Grady, N., Pitz, R., Carter, C., and Hsu, K.-Y., "UV Raman scattering measurements in reacting scramjet flows over a piloted cavity," Poster presentation, Gordon Research Conference on Laser Diagnostics in Combustion, Waterville Valley, NH, Aug. 2011.
96. Gordon, R.L., Boxx, I., Carter, C., Dreizler, A., and Meier, W., "Lifted diffusion flame stabilization: conditional analysis of multi-parameter high-repetition rate diagnostics at the flame base," *Flow, Turbulence and Combustion* **88**, 503 (2012).
97. Steinberg, A.M., Boxx, I., Stöhr, M., Meier, W., and Carter, C.D., "Effects of flow structure dynamics on thermoacoustic instabilities in swirl-stabilized combustion, *AIAA Journal* **50,** 952 (2012).
98. Tuttle, S.G., Carter, C.D., and Hsu, K-Y, "Particle image velocimetry in an isothermal and exothermic high-speed cavity," AIAA-2012-0330, 50h AIAA Aerospace Science Meeting, Nashville, TN, Jan. 2012. **Best Paper**, awarded by the *Air Breathing Propulsion Technical Committee.*
99. Lin, K.-C., Carter, C., Smith, S., Kastengren, A., "Exploration of aerated-liquid jets using x-ray holography," AIAA Paper 2012-0347, Jan. 2012.
100. Ombrello, T., Carter, C., McCall, J. Schauer, F., Tam, C.-J., Naples, A., Hoke J., and Hsu, K.-Y., "Enhanced mixing in supersonic flow using a pulse detonation combustor," AIAA Paper 2012-0123, Jan. 2012.
101. Ombrello, T.M., Carter, C.D., and Katta, V., "Laminar flame propagation enhancement by singlet molecular oxygen," AIAA Paper 2012-0380, Jan. 2012.
102. Lin, K.-C., Carter, C, Brown, M,. Smith, S., and Kastengren, A., "Investigation of near-field structures of aerated-liquid jets using x-ray radiography," presented at the ILASS Americas 24th Annual Conference on Liquid Atomization and Spray Systems, San Antonio, TX, May 2012.
103. Lin, K.-C., Carter, C, Brown, M,. Smith, S., Lee, B., Zuo, X., and Ilavsky, J., "Investigation of droplet nucleation inside a beryllium injector using small angle x-ray scattering (SAXS) technique,", presented at the ILASS Americas 24th Annual Conference on Liquid Atomization and Spray Systems, San Antonio, TX, May 2012.
104. Grady, N.R., Pitz, R.W., Carter, C.D., Hsu, K.-Y., Ghodke, C., and Menon, S., "Supersonic flow over a ramped-wall cavity flameholder with an upstream strut," In press, *Journal of Propulsion and Power.*
105. Stöhr, M., Boxx, I., Carter, C.D., Sadanandan, R., Meier, W., "Experimental study of vortex-flame interaction in a gas turbine model combustor, Accepted, *Combustion and Flame.*

106. Olinger, D.S., Lee, J., Osta, A., Sallam, K.A., Lin, K.-C., and Carter, C., “Digital holographic analysis of near-field aerated liquid jets in crossflow. Part I: Algorithm development,” To be presented at the AIAA Aerospace Sciences Meeting, Grapevine, TX, Jan. 2013
107. Olinger, D.S., Sallam, K.A., Lin, K.-C., and Carter, C., “Digital holographic analysis of near-field aerated liquid jets in crossflow. Part II: Measurements,” To be presented at the AIAA Aerospace Sciences Meeting, Grapevine, TX, Jan. 2013.
108. Li, W., Cai, J., Carter, C.D., Ryan, M.D., and Tong, C., “Three-scalar subgrid-scale mixing in a turbulent coaxial jet, “ Submitted to *Journal of Fluid Mechanics*, 2012

APPENDIX A
LIST OF ACRONYMS, ABBREVIATIONS, AND SYMBOLS

ACRONYM	DESCRIPTION
1D	one dimensional
2D	two dimensional
3D	three dimensional
AFRL	Air Force Research Laboratory
AIAA	American Institute of Aeronautics and Astronautics
APS	Advanced Photon Source
BBO	beta-barium borate
CCD	charge-coupled device
CFD	computational fluid dynamic
CMOS	complimentary metal-oxide-semiconductor
DLR	German Aerospace Center
GLR	Gas-to-liquid ratio, by mass
HTV	hydroxyl tagging velocimetry
LES	large eddy simulation
LIF	laser-induced fluorescence
PCI	phase contrast imaging
PD	pulse detonator
PIV	particle image velocimetry
PLIF	planar laser-induced fluorescence
PV	precessing vortex
Re_j	jet-exit Reynolds number
RMS	root mean square
SAXS	small angle X-ray scattering
SGS	subgrid scale
SMD	Sauter mean diameter = $\Sigma d^3/\Sigma d^2$, where d is the particle diamter
SNR	signal-to-noise ratio
TA	thermoacoustic
TDLAS	tunable diode laser absorption spectroscopy
V	Velocity
X_i	Mole fraction of stream i

Unit abbreviations

fps	frames/second
Hz	frequency, 1/s
ms	milliseconds = 10^{-3} s
m/s	meters/s
ns	nanoseconds = 10^{-9} s
ps	picoseconds = 10^{-12} s
µs	microsecond = 10^{-6} seconds
µm	micrometers = 10^{-6} m
J	Joules